A Global Diagnosis of Eddy Potential Energy Budget in an Eddy-Permitting Ocean Model

YIMING GUO, a STUART BISHOP, a FRANK BRYAN, b AND SCOTT BACHMAN

^a Department of Marine, Earth, and Atmospheric Sciences, North Carolina State University, Raleigh, North Carolina ^b National Center for Atmospheric Research, Boulder, Colorado

(Manuscript received 27 January 2022, in final form 8 April 2022)

ABSTRACT: We use an interannually forced version of the Parallel Ocean Program, configured to resolve mesoscale eddies, to close the global eddy potential energy (EPE) budget associated with temperature variability. By closing the EPE budget, we are able to properly investigate the role of diabatic processes in modulating mesoscale energetics in the context of other processes driving eddy-mean flow interactions. A Helmholtz decomposition of the eddy heat flux field into divergent and rotational components is applied to estimate the baroclinic conversion from mean to eddy potential energy. In doing so, an approximate two-way balance between the "divergent" baroclinic conversion and upgradient vertical eddy heat fluxes in the ocean interior is revealed, in accordance with baroclinic instability and the relaxation of isopycnal slopes. However, in the mixed layer, the EPE budget is greatly modulated by diabatic mixing, with air-sea interactions and interior diffusion playing comparable roles. Globally, this accounts for ~60% of EPE converted to EKE (eddy kinetic energy), with the remainder being dissipated by air-sea interactions and interior mixing. A seasonal composite of baroclinic energy conversions shows that the strongest EPE to EKE conversion occurs during the summer in both hemispheres. The seasonally varying diabatic processes in the upper ocean are further shown to be closely linked to this EPE-EKE conversion seasonality, but with a lead. The peak energy dissipation through vertical mixing occurs ahead of the minimum EKE generation by 1–2 months.

KEYWORDS: Mesoscale processes; Transport; Atmosphere-ocean interaction; Eddies; Mixing

1. Introduction

Mesoscale eddies, which have typical length scales of 10-100 km and vary on monthly and even longer time scales, are thought to provide the largest contribution to ocean variability and to dominate the oceanic kinetic energy reservoir (Ferrari and Wunsch 2009). These oceanic features can transport and mix tracers and have large impacts on ocean circulation and climate variability (Volkov et al. 2008; Chelton et al. 2011; Klocker and Abernathey 2014; Farneti et al. 2010). Baroclinic instability is thought to be a significant source of ubiquitous mesoscale eddies (Smith 2007), drawing energy from large-scale available potential energy (MPE) and converting it into eddy kinetic energy (EKE). Based on the Lorenz energy cycle (Lorenz 1955; Von Storch et al. 2012) in the ocean, a two-step path is followed to complete the energy transfers in this instability process. The conversion from MPE to EPE through downgradient eddy buoyancy fluxes is first involved in this pathway and EPE is then converted to EKE through vertical eddy buoyancy fluxes; these two stages are referred to as baroclinic conversion (BC) and potential-kinetic conversion (PKC), respectively, and account for the main production of EPE and EKE in baroclinically unstable jet systems.

As discussed by Marshall and Shutts (1981), only the BC rate associated with horizontally divergent eddy heat flux is directly related to baroclinic instability events, and the dominance of the rotational component of BC can overwhelm its dynamically important counterpart in the spatial distribution (Jayne and Marotzke 2002). A Helmholtz decomposition of

 ${\it Corresponding\ author}. \ Yiming\ Guo, yguo 20@ncsu.edu$

the horizontal flux into divergent and rotational components is necessary to partition the BC rate and extract the dynamically active part. With regional in situ observations, divergent eddy heat fluxes have been estimated in the Kuroshio Extension (Bishop et al. 2013) and Gulf Stream (Cronin and Watts 1996; Zhai and Greatbatch 2006) under two conditions following Marshall and Shutts (1981): 1) the mean velocity is aligned with the mean temperature field in the water column and 2) the rotational flux circulates around the EPE contours. However, the regional decomposition of eddy fluxes based on Marshall and Shutts (1981) may not fully separate the purely nondivergent/ nonrotational components with a residual flux (Bishop et al. 2013). Alternatively, the divergent flux can be extracted through decomposition by solving the 2D Poisson equation globally (Jayne and Marotzke 2002; Aoki et al. 2013; Guo and Bishop 2022). Associated with the two components in horizontal eddy heat flux, Marshall and Shutts (1981) proposed two one-to-one balances that can be achieved in the ocean interior when all heat sources and sinks and the eddy advection of EPE are neglected. The rotational BC component is thought to be associated with the spatial growth and decay of eddies and balances the mean flow advection of EPE (Marshall and Shutts 1981). The remaining balance is between the divergent BC and the PKC rate. Due to the limited temporal and spatial coverage of oceanic observations, this hypothesis has not yet been quantitatively tested in the global ocean.

Recent high-resolution satellite observations and coupled climate simulations have indicated that large amounts of potential energy are released from mesoscale structures to the overlying atmosphere (Ma et al. 2016; Bishop et al. 2017). Based on a regionally coupled model in the Kuroshio

Extension, Ma et al. (2016) revealed that mesoscale air-sea interactions can account for more than 70% of the removal of EPE and that more EPE can be converted into EKE through baroclinic instability when this feedback is suppressed. In Bishop et al. (2020), the mesoscale air-sea feedback was estimated based on the covariance of anomalous sea surface temperature (SST) and net heat flux (NHF) in the global ocean using observations and a high-resolution coupled climate model, and the authors demonstrated that heat exchange between mesoscale eddies and the atmosphere accounts for a global EPE sink of O(0.1) TW. However, the importance of this EPE sink from air-sea interactions to global baroclinic energy conversions and the roles of other diabatic processes in modulating the efficiency of the MPE-EKE conversion are still yet to be determined. To answer these questions, a global diagnostic analysis through a closed EPE budget in which all EPE sources and sinks are distinguished is essential.

Regional EPE budgets have been investigated in the Gulf Stream with relatively short temporal in situ records (Cronin and Watts 1996) and in the Kuroshio Extension with coupled simulations (Yang et al. 2019). Von Storch et al. (2012) performed ocean-only simulations to quantify global oceanic energetics and suggested that the energy exchanges between different energy reservoirs are dominated by the baroclinic pathway. While their pioneering works have improved our knowledge on ocean energy cycles, some aspects regarding EPE remain unclear and are further explored in this work. First, we adopt a different definition of "eddy" as an anomaly relative to monthly climatology instead of the deviations from ensemble time means used in model-based global studies (Von Storch et al. 2012) and observational-based regional estimates (Cronin and Watts 1996). The average seasonal cycle is a forced repeatable pattern and is not associated with ocean internal variability. It has been shown that the inclusion or omission of the seasonal cycle in eddy terms can change the sign of EPE generation by air-sea interactions (Bishop et al. 2020). Second, the global geographic and vertical structures of dynamically important BC rates have not yet been fully quantified. The decomposition on eddy heat flux into divergent and rotational components has been shown to be necessary for local energetics analysis (Guo and Bishop 2022). In previous budget diagnoses (e.g., Von Storch et al. 2012), no partition was applied for the energy conversion from MPE to EPE (BC), and the strong rotational flux in the frontal regions caused the actual downgradient flux to be unclear. By applying the decomposition, the balances proposed under the quasigeostrophic and adiabatic framework in Marshall and Shutts (1981) can be examined with a realistic model. Third, and more importantly, the relative roles of air-sea interaction and other diabatic processes (i.e., diffusion) on three-dimensional EPE dissipation remains unknown globally.

In this work, we seek to examine the abovementioned issues by carrying out an investigation of the global EPE budget of a 1/10° interannually forced ocean model simulation that is configured to resolve mesoscale eddies. Notably, the EPE equation based on the ocean buoyancy field is not directly used. Instead, the tracer-variance equation, which is closely related to the EPE equation, is adopted here. This is because

the density field is determined based on temperature and salinity via the equation of state (McDougall et al. 2003), and density-related fluxes are not archived in the model output used in the analysis. The model provides all relevant heat and salinity fluxes every 5 days such that the temperature and salinity equations are strictly closed, respectively. Therefore, to maintain the high-frequency variability as much as possible with the existing simulations, we carry out EPE analysis using tracer variance equations. Furthermore, considering the relatively weak role salinity plays in eddy energetics (see a regional comparison in Yang et al. (2019) and appendix B in this work) and previous studies that successfully used the temperature anomaly as a proxy for the density anomaly (i.e., Luecke et al. 2017), we only consider the thermal component and use the temperature variance (T-variance) equation as a proxy of the EPE equation to focus on EPE that is associated with temperature variability (hereinafter referred to as T-EPE).

The structure of the rest of the paper is as follows. Section 2 gives a brief description of the model data and methods used in the analysis. The main results are presented in section 3. The conclusions are summarized in section 4.

2. Data and method

a. Model simulation

The ocean simulation presented here uses the Parallel Ocean Program (POP), version 2 (Smith et al. 2010) in an eddy-resolving oceanic tripole grid (poles in North America and Asia) with 62 vertical levels (10-m resolution above 160 m and gradually increasing to 250 m toward the sea floor) and a nominal horizontal resolution of 0.1° (11 km at low latitudes and 2.5 km at high latitudes), which is sufficient to resolve the most energetic scales of mesoscale variability and can even capture some submesoscale processes (Uchida et al. 2017). The model topography was adapted from ETOPO2 and partial bottom cells (Adcroft et al. 1997; Pacanowski and Gnanadesikan 1998) were implemented to improve topographic interaction with flows. A second-order centered difference advection scheme for both horizontal momentum and tracers is used in POP. The nonlocal K-profile parameterization (KPP) scheme (Large et al. 1994) was applied to parameterize the surface mixed layer and interior vertical mixing processes. Horizontal mixing by subgrid scales was parameterized using biharmonic operators. The viscosity and diffusivity values vary spatially with the cube of the local grid spacing and have equatorial values of 2.7×10^{10} and $3 \times 10^9 \,\mathrm{m}^4 \,\mathrm{s}^{-1}$, respectively.

The model configuration was similar to that used in Bryan and Bachman (2015) except that it employed a different forcing profile. The model used in this paper was forced by the Japanese 55-year Reanalysis (JRA55) data (Kobayashi et al. 2015). The JRA55 dataset, conducted by the Japan Meteorological Agency (JMA), is composed of atmospheric reanalysis and remote sensing products and based on JMA's operational global data assimilation–forecast system. Observations used in the JRA dataset primarily come from ERA-40 and other observational products archived by the JMA. This dataset originally uses a reduced TL319 (~55 km) grid and is interpolated

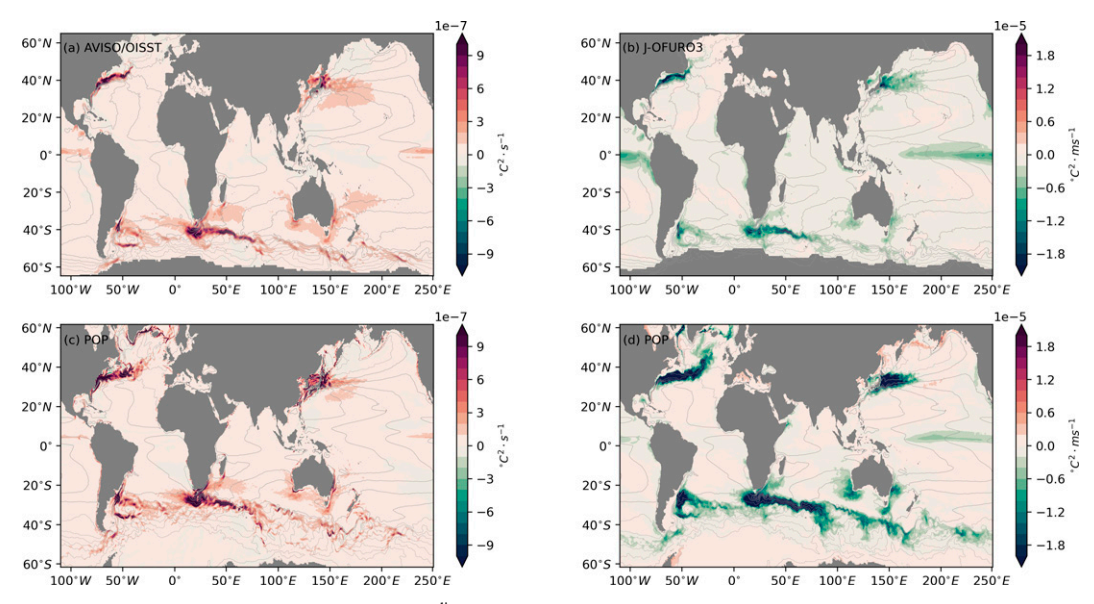


FIG. 1. Surface estimates of divergent BC $_T^{\text{div}}$ and T-OMEA with satellite observations and forced POP model. (a),(c) The surface T-EPE conversion $(-\overline{\mathbf{u}_h'}T'^{\text{div}} \cdot \nabla \overline{T})$ from observations and the model, respectively. The EPE dissipation through air–sea interaction $(\overline{T'Q'}/\rho_o C_p)$ is computed based on (b) J-OFURO3 and (d) the model (adapted from Bishop et al. 2020). Gray contours are mean SSH with a contour interval of 20 cm.

onto the normal TL319 grid for forcing ocean models at 3-h intervals (Tsujino et al. 2018). The ocean is forced by the fluxes of momentum, heat, and freshwater. The momentum fluxes are computed with the bulk formula that relates the fluxes to wind speed and drag coefficient. The freshwater fluxes include evaporation, precipitation, and river runoff. The heat fluxes are composed of fluxes at the ocean-atmosphere surface and ocean-ice surface, as well as heat transport due to runoff. At the air-sea interface, the heat flux is a combination of shortwave, longwave, and turbulent latent and sensible heat fluxes. Detailed formulations to calculate the surface fluxes in JRA55 data are thoroughly summarized in Tsujino et al. (2018) in their section 2. The model simulation used in this work spans the period 1958-2018 and is initialized at rest with temperature and salinity distributions from the World Ocean Atlas 2013 (Boyer et al. 2013). Our analysis in this study is based on this interannually forced model output from 1999 to 2018 (model period of year 42 to year 61) with heat and salinity budget terms (i.e., heat fluxes $\mathbf{u}_h T$, wT) accumulated and saved every 5-day besides standard model output.

b. Observational datasets

Three observational datasets are used to produce Fig. 1: sea surface height (SSH) and geostrophic velocity, SST, and surface net heat flux (NHF). The SSH and geostrophic velocity dataset is provided by the Archiving, Validation and Interpretation of Satellite Oceanographic (AVISO) and is available daily from 1992 on a $0.25^{\circ} \times 0.25^{\circ}$ grid. The data used are for the temporal period from January 1993 to December 2017. The SST dataset is on a $0.25^{\circ} \times 0.25^{\circ}$ grid of version 2 of the Optimum Interpolation SST product (OISSTv2) (Reynolds et al. 2007) provided by the National Oceanic and Atmospheric

Administration (NOAA). The same period as the SSH dataset is used for the SST. The NHF data, which have the same horizontal resolution as SSH and SST, are from monthly mean product of J-OFURO3, a third-generation dataset developed by the Japanese Ocean Flux Datasets with Use of Remote sensing Observations (J-OFURO) and includes shortwave, longwave, and turbulent latent and sensible heat fluxes (Tomita et al. 2019).

c. T-variance equation

The *T*-variance equation for an incompressible Boussinesq fluid used in this analysis can be written as

$$\frac{\frac{\partial}{\partial t} \left(\overline{T'^2} \right)}{\text{TEND}} = \underbrace{-\overline{u'_h T'} \cdot \nabla_h \overline{T}}_{\text{TEND}} BC_T \underbrace{-\overline{w' T'}}_{\text{DE}} \frac{\frac{\partial}{\partial \overline{T}}}{\frac{\partial}{\partial z}} PKC_T \underbrace{-\overline{\mathbf{v}} \cdot \overline{\nabla} \left(\overline{T'^2} \right)}_{\text{ADV}} + \underbrace{\overline{T'} \frac{\partial}{\partial z} \left[\kappa \left(\frac{\partial T'}{\partial z} - \Gamma' \right) \right]}_{\text{VMIX}} + \underbrace{\overline{T'} \frac{\partial}{\partial z} \left(\overline{Q'_{\text{sw}}}_{\rho_o C_p} \right)}_{\text{HDIFF}} \underbrace{-\overline{T'} A_h \overline{\nabla}^4 T'}_{\text{HDIFF}},$$
(1)

with surface boundary condition

$$\left[\kappa \frac{\partial T'}{\partial z}\right]_{z=0} = \frac{Q'_o}{\rho_o C_p},\tag{2}$$

where T is potential temperature, $\mathbf{u}_h = (u, v)$ is the horizontal velocity vector, w is the vertical velocity, ∇_h denotes the horizontal gradient operator, κ is the molecular diffusivity, Γ represents the countergradient flux of temperature as predicted by KPP, $Q_{\rm sw}$ is the forcing by the shortwave radiation, ρ_o and C_p are the constants of a reference ocean density and heat

capacity of the ocean, A_h is the horizontal diffusivity, and Q_o is the net nonsolar surface heat flux. Here we use a Reynolds operator (·), which represents a temporal averaging of the model output [here the averaging refers to the monthly climatology from the model output following Bryan et al. (2014), Griffies et al. (2015), and Bishop et al. (2020)]. Deviations from this average will be denoted by a prime $(\cdot)'$. The sensitivity of major terms in Eq. (1) to the definition of eddy was tested using two other methods, such as 1) filtering the raw data to only keep the variability within one year, which is a typical scale that contains most ocean mesoscale variability, and 2) removing the long-term mean following traditional Reynolds decomposition, as was adopted in previous studies (Von Storch et al. 2012; Chen et al. 2014). By examining these two different definitions, we recomputed the energy conversion terms in Eq. (1) in the Kuroshio Extension and Gulf Stream (not shown), and we did not find significant differences from the method that was used in this work. Instead, the method used here relaxes the computational burden of applying filter operations on a 1/10° global grid. However, Bishop et al. (2020) showed that the traditional definition of an eddy as a deviation from the long-term mean does not accurately reflect their true role in the generation of EPE through air-sea interactions, emphasizing the necessity of isolating internal ocean processes from the forced seasonal cycle. Therefore, to correctly represent the mesoscale air-sea interaction on the surface, it is better to remove the monthly climatology given that it does not largely affect internal energy conversions.

Different processes driving the T-variance variation are described in the underbraces. The tendency of T-variance over time, TEND, is on the left-hand side of Eq. (1). On the righthand side, for brevity, we group the horizontal and vertical advection of mean and eddy flow into the three-dimensional vector operator $\mathbf{v} \cdot \nabla = (\overline{\mathbf{u}_h} + \mathbf{u}_h') \cdot \nabla_h + (\overline{w} + w') \partial / \partial z$, and denote it as ADV. Baroclinic conversions from MPE to EPE associated with temperature variability (BC_T) are represented by the horizontal eddy heat flux acting on the mean thermal gradient. The following conversion into EKE through baroclinic instability from the thermal contribution is termed as PKC_T in the T-variance equation. The vertical mixing, denoted as VMIX, includes the vertical diffusion of T-variance, the countergradient KPP flux, and heating from penetrating solar radiation. HDIFF refers to horizontal diffusion. Detailed derivations of Eq. (1) are given in appendix A.

As shown in Marshall and Shutts (1981), the baroclinic conversion can be partitioned into rotational (BC $_T^{\text{rot}}$) and divergent (BC $_T^{\text{div}}$) components, where the rotational part does not play a dynamical role and can be balanced by the mean advection of T-variance. The energy conversion from T-MPE to T-EPE is thus represented by BC $_T^{\text{div}}$. This divergent-rotational decomposition on BC $_T$ is completed through applying a Helmholtz decomposition on the eddy heat flux,

$$\mathbf{u}_{h}'T' = \underbrace{\mathbf{k} \times \nabla \psi}_{(\mathbf{u}_{h}'T')^{\text{tot}}} + \underbrace{\nabla \phi}_{(\mathbf{u}_{h}'T')^{\text{div}}}, \tag{3}$$

where **k** is the vertical unit vector, ψ is the vector potential, and ϕ is the scalar potential. The curl of ψ is regarded as the

rotational component and the divergence of ϕ indicates the divergent component. This decomposition of the ocean eddy heat flux can be achieved through solving 2D Poisson equation and has been applied on regional (Abernathey and Cessi 2014) and global studies (Jayne and Marotzke 2002; Aoki et al. 2013). More discussions on the decomposition can be found in Guo and Bishop (2022). The baroclinic conversion associated with the heat flux can then be partitioned as

$$BC_{T} = \underbrace{-\left(\overline{\mathbf{u}_{h}^{\prime}T^{\prime}}\right)^{\text{rot}} \cdot \nabla \overline{T}}_{BC^{\text{div}}} \underbrace{-\left(\overline{\mathbf{u}_{h}^{\prime}T^{\prime}}\right)^{\text{div}} \cdot \nabla \overline{T}}_{BC^{\text{div}}}.$$
 (4)

With this decomposition on BC $_T$, the T-variance equation at a particular depth can be written as

$$\underbrace{\frac{\partial}{\partial t} \left(\overline{T'^{2}} \right)}_{\text{TEND}} = \underbrace{- \underbrace{\mathbf{u}'_{h} T'^{\text{rot}} \cdot \nabla_{h} \overline{T}}_{\text{BC}_{T}^{\text{rot}}} \underbrace{- \underbrace{\mathbf{u}'_{h} T'^{\text{div}} \cdot \nabla_{h} \overline{T}}_{\text{BC}_{T}^{\text{div}}} \underbrace{- \underbrace{\mathbf{w}' T'}_{\text{BC}_{T}^{\text{rot}}} \underbrace{\frac{\partial \overline{T}}{\partial z}}_{\text{PKC}_{T}}}_{\text{PKC}_{T}}$$

$$\underbrace{- \mathbf{v} \cdot \nabla \left(\overline{T'^{2}} \right)}_{\text{ADV}} + \underbrace{T' \frac{\partial}{\partial z} \left[\kappa \left(\frac{\partial T'}{\partial z} - \Gamma' \right) \right]}_{\text{VMIX}} + \underbrace{T' \frac{\partial}{\partial z} \left(\underline{Q'_{\text{sw}}}_{\rho_{o} C_{p}} \right)}_{\text{VMIX}}$$

$$\underbrace{- \overline{T' A_{h} \nabla^{4} T'}}_{\text{HDIFF}}, \tag{5}$$

with surface boundary condition

$$\left[\kappa \frac{\partial T'}{\partial z}\right]_{z=0} = \frac{Q'_o}{\rho_o C_p}.$$
 (6)

All underbraced terms in Eq. (5) will be diagnosed in the analysis that follows.

3. Results

a. Model diagnosis of conversions and sinks of T-EPE

The mesoscale variability in 1/10° POP model on a tripolar grid has been validated in a variety of studies, such as by estimating eddy heat fluxes in the Eastern Pacific (Abernathey and Wortham 2015) and the Kuroshio Extension (Bishop and Bryan 2013) and diagnosing the salinity budget (Bryan and Bachman 2015; Johnson et al. 2016) and heat budget in the tropical Pacific (Deppenmeier et al. 2021). All these studies have demonstrated the consistency between the model and available observations. More recently, global comparisons of basic climate variables from four different ocean models (including 1/10° POP used in our work) with the same configuration were given by Chassignet et al. (2020), who assessed ocean eddy kinetic energy, temperature variance, heat transport and other variables associated with ocean variability in the models by comparison with a variety of observations. Because the main focus of this work is on the ocean EPE budget, in this section we will only show the comparison of energy conversion/generation terms associated with potential energy that can be estimated with available satellite observations.

The surface eddy horizontal heat flux associated with geostrophic currents can be estimated with SSH and SST

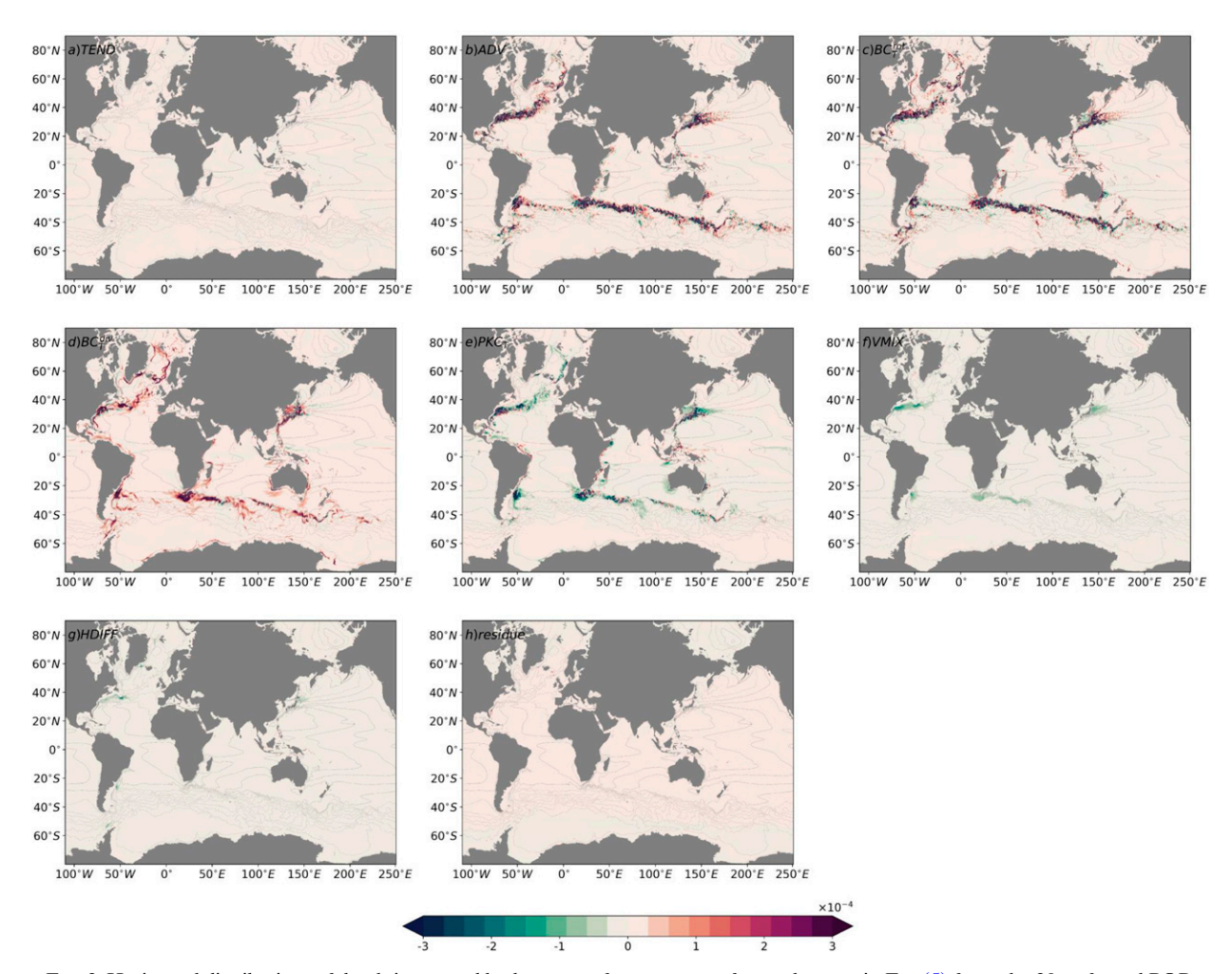


FIG. 2. Horizontal distributions of depth-integrated budget terms from ocean surface to bottom in Eq. (5) from the 20-yr forced POP simulation (${}^{\circ}\text{C}^{2}\text{ m s}^{-1}$). Gray contours are mean SSH with a contour interval of 20 cm.

observations (Abernathey and Wortham 2015; Guo and Bishop 2022). The model's performance on simulating eddy heat transport can be evaluated by comparing the surface estimates of the downgradient eddy heat fluxes with observations, as shown in Figs. 1a and 1c, which plot the global surface BC_T^{div} obtained from the observations and model, respectively. The surface estimates indicate prominent poleward eddy heat transport around the midlatitude western boundary currents and the Antarctic Circumpolar Current. Such a surface pattern suggests that energy flows from MPE to EPE (positive BC_T^{div}) in the most baroclinically unstable jets, as would be expected due to baroclinic instability. In addition to the midlatitudes, a hotspot along the equatorial Pacific can be observed in both the observations and model; this hotspot may arise from tropical instability waves with a period of about 30 days (Jayne and Marotzke 2002). In general, the model shows good agreement with observations regarding the geographic distributions of this surface divergent baroclinic energy conversion. In terms of the magnitude, the surface BC_T^{div} in the model has a relatively higher mean value of $5.8\times 10^{-8}\,^{\circ}\text{C}^2\,\text{s}^{-1}$ compared with the observed value of 5.0×10^{-8} °C² s⁻¹ within 60°S-60°N. Notably,

when using altimetry data, only geostrophic circulation is included in the eddy flux estimates.

In a process adapted from Bishop et al. (2020), we computed the covariance of net heat flux anomaly and SST anomaly to measure the thermal exchange that occurs through ocean mesoscale air-sea interactions (T-OMEA). The global distributions of this quantity obtained from observations and the model are shown in Figs. 1b and 1d, respectively. The T-OMEA feedback acts as a global T-EPE sink (Bishop et al. 2020) in both the observations and model. This effect is much stronger in the model, with a global mean value of -1.8×10^{-8} °C² m s⁻¹ compared with the observed value of -1.0×10^{-8} °C² m s⁻¹. In both the observations and model, the close correspondence of EPE destruction through T-OMEA to the conversion of EPE from MPE via BC_T^{div} on the surface suggests that some amount of EPE that should be available for conversion into EKE would be dissipated by diabatic processes such as air-sea interactions. A detailed discussion on this effect is provided in section 3d. Overall, the surface energy conversion from MPE to EPE and the EPE sink from air-sea interactions induced by temperature variability in the forced model are

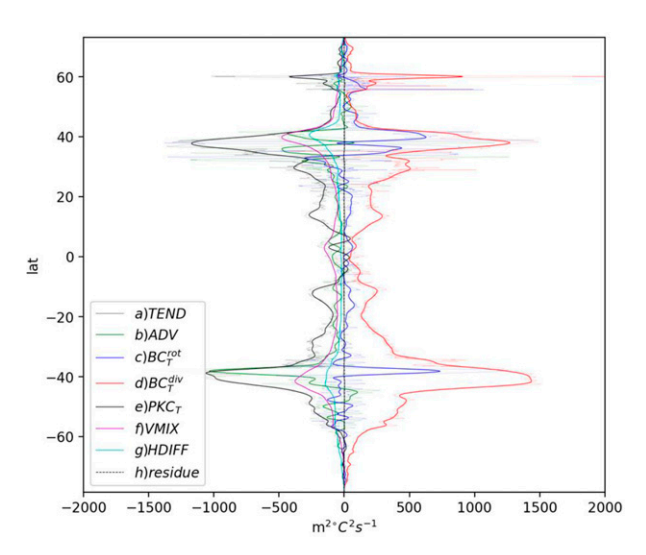


FIG. 3. The distributions of zonally and vertically integrated terms in Eq. (5). The thick solid lines indicate the distributions after applying a smoothing operator (1D Gaussian filter with length of 1°) to the original distributions (thin dashed lines).

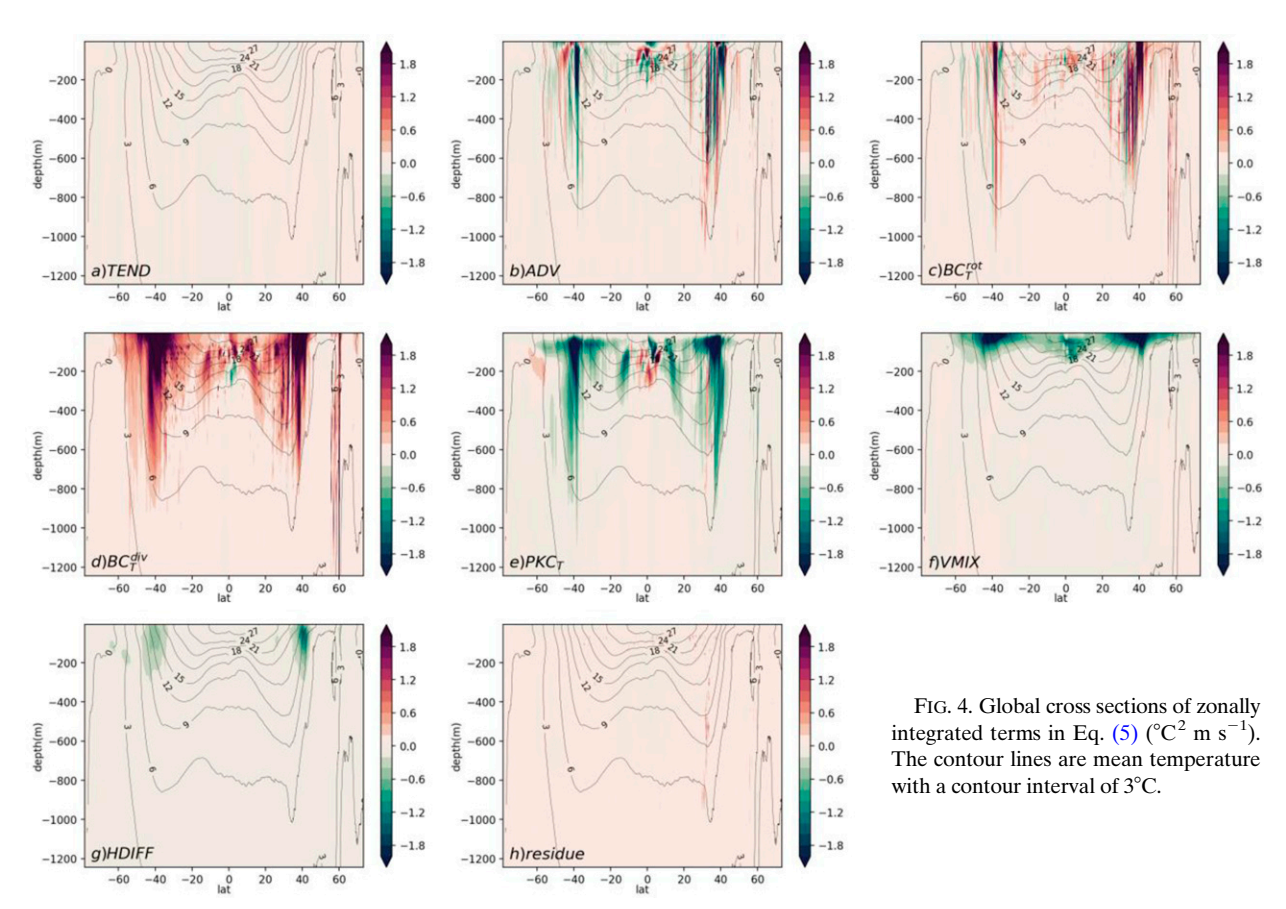
comparable to those found in the observations. However, the extent of EPE dissipation resulting from diabatic processes is undetermined by observations and can only be evaluated with numerical models.

b. Global budget

To examine the significance of different dynamical processes driving T-EPE variation, we diagnose each term listed in Eq. (5) with the forced POP model. The depth-integrated budget terms are shown in Fig. 2, and their corresponding zonal distributions are given in Fig. 3 after integrals are applied along zonal sections. Each term is computed explicitly, and we successfully close the budget with a trivial residual in Eq. (5) using 5-day model outputs (see Figs. 2h and 3). On the left-hand side of Eq. (5), the tendency of T-EPE is negligible over a 20-yr period (Fig. 2a), and this term barely contributes to the budget in all zonal sections (Fig. 3). Figure 2b shows the total T-EPE advection by both the mean and eddy velocities. The spatial distributions display zonally propagating patterns with series of positive and negative eddy-like structures that can cancel each other out to a large extent in the zonal direction; in these distributions, the global zonal values oscillate around the zero-line at different latitudinal sections (Fig. 3). The two components (rotational and divergent) of baroclinic conversion (BC_T) are shown in Figs. 2c and 2d, respectively. The original distribution of BC_T before partitioning has a wavelike structure, a similar pattern to that shown in the advection term, with positive and negative values alternatively occurring due to the meandering characteristics of oceanic zonal jets. This spatial structure is caused by the rotational eddy heat flux and is most prominent in regions of zonally meandering currents (Jayne and Marotzke 2002), as shown in Fig. 2c. However, the rotational component does not truly contribute to the global budget with the actual dynamics in its

divergent counterpart. BC_T^{div} exhibits a smooth distribution, with generally positive values in all regions, indicative of the conversion from MPE to EPE. The EKE generation through baroclinic instability is quantified in the PKC_T term, and the vertically integrated distribution of this process is shown in Fig. 2e. Globally, this upgradient vertical eddy heat flux shares a similar geographic distribution with the downgradient horizontal flux, and the spatial patterns of both of these quantities suggest strong eddy activity in the midlatitude western boundary currents and the Antarctic Circumpolar Current (Fig. 3). In addition, vertical diffusion plays a role as an energy sink and can greatly modulate energy conversions in the most energetic regions (Fig. 2f). The most prominent vertical dissipation occurs in the midlatitudes and tropics, where the strongest energy conversions (as in Figs. 2d, 2e, and 3) exist. This vertical mixing dominates the total diffusion in the horizontal and vertical directions (Figs. 2f,g), although a small amount of T-EPE can also be destroyed through horizontal mixing (Fig. 3).

A representation of the global vertical structure of each term in the T-EPE equation, obtained by zonally integrating over all longitudes, is indicated in Fig. 4, showing how different dynamical processes regulate the T-EPE variability in the water column. With relatively steady turbulence over 20 years, the TEND values are quite small at all depth levels. The ADV and BC_T^{rot} terms have similar vertical distributions but opposite signs in most areas (Figs. 4b,c). These two terms can eventually compensate for each other to a large extent and do not largely contribute to EPE changes globally. The large internal cancellation between advection of EPE and rotational baroclinic conversion is achieved with two conditions, as discussed in Marshall and Shutts (1981). First, the rotational flux, which is associated with the spatial growth and decay of eddies, circulates around the temperature variance. This relationship is verified in the Kuroshio Extension (Bishop et al. 2013) and Gulf Stream (Cronin and Watts 1996) with full-depth in situ observations, and in the global mixed layer with surface satellite observations and a highresolution climate simulation (Guo and Bishop 2022). Second, the mean velocity follows the mean temperature contours, as demonstrated in Marshall and Shutts (1981), and it infers that there is a linear relationship between the geostrophic streamfunction and temperature field (Killworth 1992; Cronin and Watts 1996; Bishop et al. 2013). With these two conditions, it is straightforward to show that BC_T^{rot} is approximately balanced by ADV as derived in Marshall and Shutts (1981) in their section 3. The necessarity of partitioning the baroclinic conversion into rotational and divergent components is also discussed in Chen et al. (2014); Kang and Curchitser (2015) with a different interpretation from the perspective of regional eddy-mean flow interactions. Their work, which only estimated ocean internal energy transfers between potential and kinetic reservoirs for both mean and eddy circulations instead of fully closing energy budgets, shows that the "nonlocal" processes (i.e., advection, air-sea interactions) play a nontrivial role in eddy-mean flow energy conversions in typical baroclinically unstable regions, such as the Kuroshio, Gulf Stream, and Southern Ocean (Chen et al. 2014). The

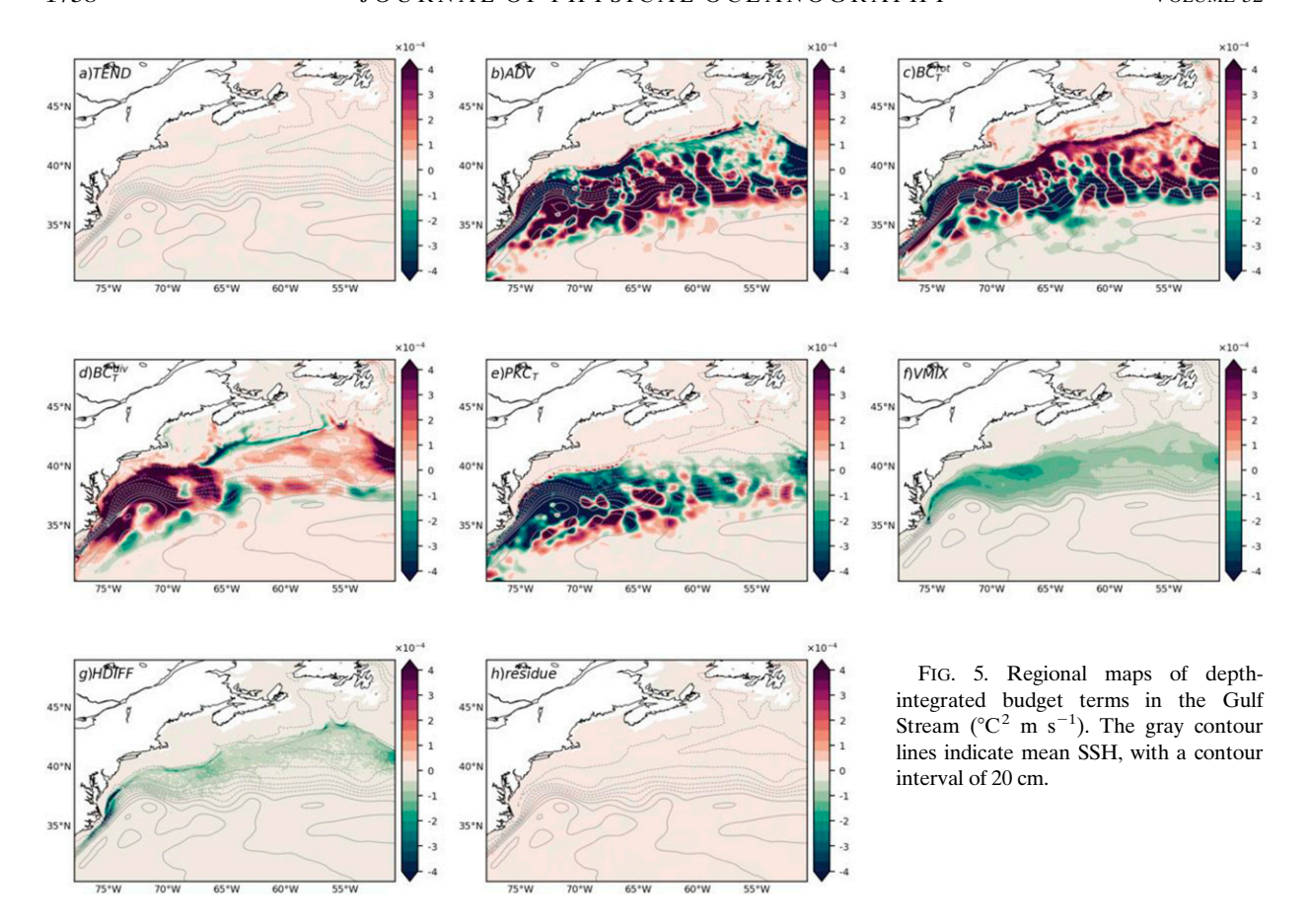


BC_T^{rot} computed in our work is part of these nonlocal processes, which is nonnegligible in regional energy budgets (Cronin and Watts 1996; Bishop et al. 2013; Zhai and Greatbatch 2006). Regarding the most significant generation of T-EPE, a global cross section of the downgradient divergent eddy heat flux from POP model is shown in Fig. 4d. The BC_T^{div} term exhibits surface-intensified vertical distributions in the midlatitudes and reaches a maximum in the subsurface in low-latitude regions. Figure 4e shows the vertical distribution of PKC_T, which is associated with the upgradient vertical flux. The strong eddy energy conversions can penetrate as deep as 800 m in the midlatitudes and occurs in regions with large thermal gradients (as indicated by closeness of the contour lines in Fig. 4). In addition to its horizontal distribution, BC_T^{div} is also spatially coherent with the PKC_T in the vertical except for a very weak vertical heat flux in the mixed layer (Fig. 4e). The weaker energy conversion between T-EPE and EKE on the ocean surface correspond to surface-intensified vertical mixing, as shown in Fig. 4f. The VMIX term reveals that the EPE dissipation that occurs through vertical thermal diffusion is mostly confined to the upper ocean, where the heat exchange between the atmosphere and ocean eddies plays an important role (Ma et al. 2016; Bishop et al. 2020). The horizontal diffusion process (Fig. 4g) is shown to be less significant than the vertical

mixing term, and the HDIFF only exhibits large values in a narrow zonal band in the midlatitudes in the upper 200 m. In general, the main balance in Eq. (5) occurs among $BC_T^{\rm div}$, PKC_T, and VMIX, as shown in Figs. 4d–f, with relatively small contributions from other processes.

c. Regional variability

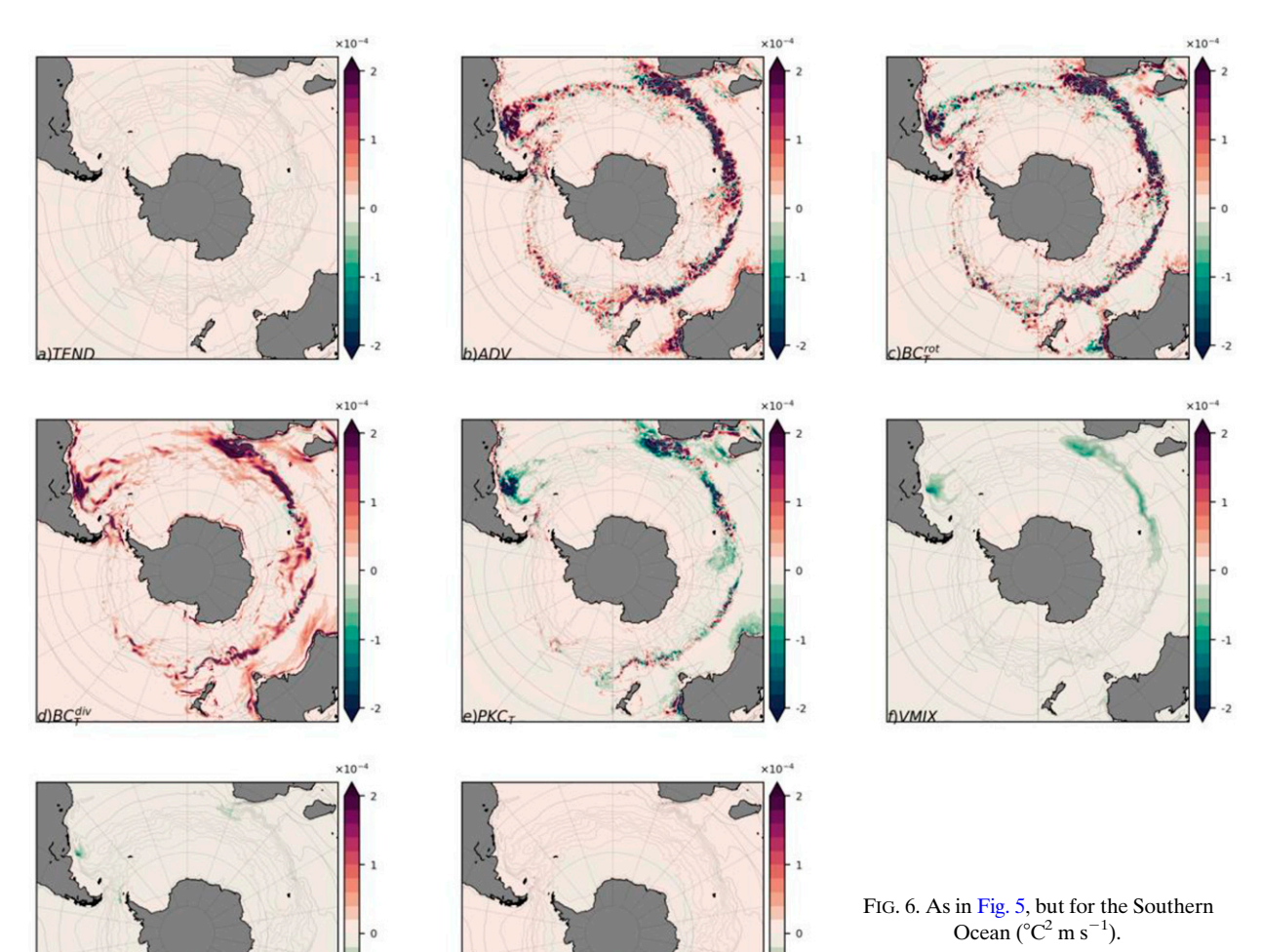
The local T-EPE budget terms for the Gulf Stream are shown in Fig. 5. Based on the vertically integrated spatial distributions of the terms in Eq. (5), the significant processes driving the local rate of change in T-EPE are ADV, BC_T^{rot} , BC_T^{div} , PKC_T , and VMIX, each of which has a clear spatial structure. Among these terms, the wavelike pattern is most prominent in the BC_T^{rot} term, which is spatially related to the ADV term. As proposed in Marshall and Shutts (1981), the rotational eddy heat flux is indicative of the spatial growth and decay of eddies and balances the mean advection of T-variance when the advection by the eddy velocity is neglected. In Figs. 5b and 5c, the signal of this relationship, as described in Marshall and Shutts (1981), is shown for the Gulf Stream; however, the BC_T^{rot} term does not balance the mean advection precisely, as the triple correlation term (eddy advection) may also play a role in regions where the Rossby number is not small. In an adiabatic scenario, a nearly one-



to-one balance between $\mathrm{BC}_T^{\mathrm{div}}$ and PKC_T was inferred in Marshall and Shutts (1981). As shown in the Gulf Stream, the local BC_T^{div} is spatially coherent with PKC_T , and both are aligned with the mean SSH gradient (Figs. 5d,e). The different signs of BC_T^{div} and PKC_T indicate that horizontal eddy heat fluxes act to weaken the background temperature gradient and that the vertical thermal structure can be restratified through vertical eddy fluxes. Although their spatial patterns share many similarities, the magnitude of BC_T^{div} is larger than that of PKC_T in some areas. In addition, this magnitude mismatch can be largely explained by the strong diabatic mixing occurring along the jets (Figs. 5f,g). Compared with the horizontal diffusion term HDIFF, the vertical mixing VMIX plays a larger role in energy dissipation along the western boundary currents as found in the Kuroshio Extension (not shown) and Gulf Stream (Fig. 5). In these regions, the distributions of VMIX mostly concentrate on the poleward side of the western boundary currents, as shown in the example given in Fig. 5f. Bishop et al. (2020) also captured these characteristics in their estimates of mesoscale air-sea interactions using the covariance of anomalous SST and net heat fluxes obtained from satellite observations. This pattern potentially implies that the warm eddies on the colder side of the zonal currents release larger amounts of potential energy when exposed to the much colder and drier overlying atmosphere (Yang et al. 2019). Moreover, the spatial patterns of VMIX are generally

associated with the $\mathrm{BC}_T^{\mathrm{div}}$, with larger energy conversions corresponding to stronger energy dissipation. For example, in the Gulf Stream, $\mathrm{BC}_T^{\mathrm{div}}$ and VMIX share two regional hotspots: one is located near the large meander after the Gulf Stream separates off Cape Hatteras and extends to the region off Cape Cod (Fig. 5d); the other is further downstream on the eastern boundary of the domain shown in Fig. 5. The horizontal spatial coherence among $\mathrm{BC}_T^{\mathrm{div}}$, PKC_T , and VMIX suggests a nearly three-way balance in modulating local T-EPE variations.

In Fig. 6, we show the regional T-EPE budgets for the Southern Ocean. The horizontal structures of the depthintegrated terms are generally located along the Antarctic Circumpolar Current path, as indicated by the large SSH gradient, and the western boundary currents and their extensions dominate the majority of the T-EPE sources and sinks. Similar to the conditions seen in the Gulf Stream, ADV and BC_T^{rot} are spatially correlated with each other and barely contribute to the integrated energy. The aforementioned three-way balance appears in the Southern Hemisphere as well, with the energy conversions (Figs. 6d,e) in the most turbulent regions modulated by the VMIX term (Fig. 6f). The strongest energy dissipation through vertical mixing is seen in the Agulhas Return Current and Brazil-Malvinas Confluence, where the most prominent energy conversions occur.



d. Role of air-sea interaction

We have shown above that vertical mixing plays a significant role in regulating the baroclinic pathway based on a global T-EPE diagnosis. Notably, in Eq. (5), the VMIX term includes all processes that together contribute to the vertical dissipation of T-EPE in the model prognostics. Here we further decompose this term into three components related to air–sea interactions (VMIX $_{a-s}$), diffusive mixing (VMIX $_{diff}$) and countergradient fluxes in KPP scheme (VMIX $_{kpp}$). These three components are partitioned as

$$VMIX = \underbrace{\overline{T'\frac{\partial}{\partial z} \left(\frac{Q'}{\rho_o C_p}\right)}}_{VMIX_{a-s}} + \underbrace{\overline{T'\frac{\partial}{\partial z} \left(\kappa\frac{\partial T'}{\partial z}\right)}}_{VMIX_{diff}} + \underbrace{\overline{T'\frac{\partial}{\partial z} \left(\kappa\Gamma'\right)}}_{VMIX_{kpp}}, \quad (7)$$

where Q is a combination of surface nonsolar net heat flux Q_o and the penetrative radiation $Q_{\rm sw}$. We adopt zero surface boundary conditions for the latter two terms in Eq. (7). The

total VMIX is shown on the top panel of Fig. 7a in the same form as the plot in Fig. 2f, but with a different color scale. This energy destruction through mesoscale air-sea interaction (Fig. 7b) generally dominates the global geographic patterns of VMIX, with large concentrations on the midlatitudes and tropics. The mixing associated with the vertical diffusive flux is relatively weaker than the air-sea feedback, and regional hotspots from VMIX_{diff} are found on the poleward side of western boundary currents and along the equator (Fig. 7c). In addition, a portion of the energy dissipation is completed by the vertical nonlocal flux in the KPP scheme for the vertical turbulent heat flux. The effect of countergradient fluxes introduced by KPP in VMIX is evaluated in Fig. 7d, and the VMIX_{kpp} term is found to be mostly concentrated along the western boundary currents. Based on the zonal integrals of the three components shown in Fig. 8, VMIX_{a-s} plays the largest role in destroying T-EPE, with zonal maximums in the midlatitudes and tropics. In the Northern Hemisphere, all three components in VMIX reach local maximums near 40°N,

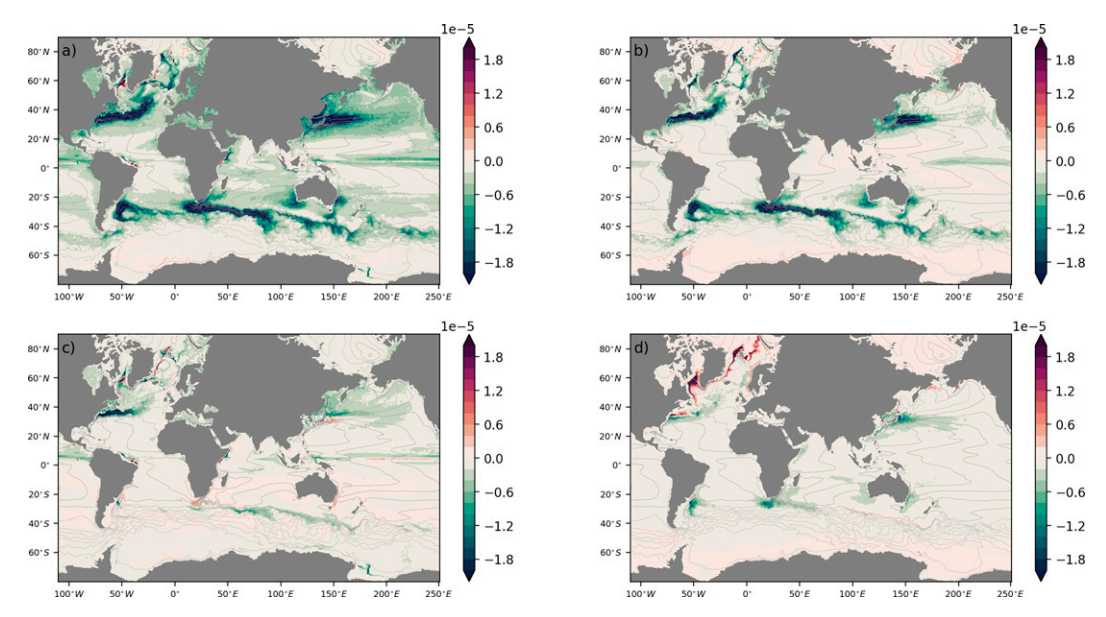


FIG. 7. The horizontal distributions of (a) total vertical mixing and its three components related to (b) air–sea interaction, (c) diffusive flux, and (d) countergradient flux in KPP, after vertically integrating from the surface to the bottom (${}^{\circ}C^{2}$ m s⁻¹). Gray contours are mean SSH with a contour interval of 20 cm.

and the zonal integrals of VMIX $_{\rm diff}$ and VMIX $_{\rm kpp}$ are slightly offset from that of VMIX $_{\rm a-s}$ to the north and south, respectively. Near the equator, the VMIX $_{\rm diff}$ term is the strongest quantity compared with the contributions from air–sea interactions and countergradient fluxes from KPP. In the Southern Hemisphere, the VMIX $_{\rm diff}$ term induces the smallest portion of T-EPE sink around 40°S, with over 70% of the total destruction coming from air–sea interactions VMIX $_{a-s}$. Globally, the interior vertical mixing including both VMIX $_{\rm diff}$ and VMIX $_{\rm kpp}$ (~0.16 TW) has a comparable magnitude with the mesoscale air–sea feedback VMIX $_{\rm a-s}$ (~0.17 TW). The unit conversions are described in the following discussion section.

The cross sections of vertical mixing and its three components are shown in Fig. 9. The VMIX process is mostly confined to the upper 200 m, with air–sea interactions (Fig. 9b) playing the largest role near the surface. In the midlatitudes, the surface-intensified vertical mixing is dominated by the

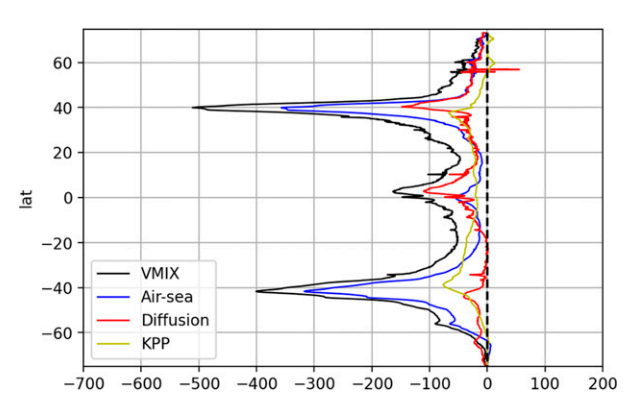


FIG. 8. Zonally and vertically integrated three components in VMIX (${}^{\circ}\text{C}^2\text{ m}^2\text{ s}^{-1}$).

mesoscale air-sea energy sink even though the positive VMIX_{diff} and VMIX_{kpp} near the surface compensate for part of the surface destruction. In the tropics, the T-EPE sink induced by VMIX_{a-s} is partly canceled out by the positive VMIX_{diff}, resulting in a very weak negative VMIX near the surface (Fig. 9). The opposite effect of solar penetrative flux and vertical diffusion on cross-isothermal motions is demonstrated in the near-surface equatorial Pacific (Deppenmeier et al. 2021). From the perspective of eddy energetics in this study, the mesoscale air-sea interaction acts to destruct eddy energy, while the near-surface turbulence VMIX_{diff} tend to oppose this effect. But the surface sink of T-EPE in VMIX $_{a-s}$ exceeds the magnitude of positive VMIX_{diff}, leading to an overall negative signal in surface VMIX. Deeper in the surface layer the $VMIX_{diff}$ and $VMIX_{kpp}$ terms are the only two sources for vertical mixing except for a small contribution from solar penetrative radiation in VMIX_{a-s}. The impact of downward solar heat radiation flux reduces with depth and is negligible below 50 m (Fig. 9b). In the midlatitudes, the countergradient flux induced by KPP (Fig. 9d) has the largest influence on the sink of EPE below the surface and shows symmetric vertical structures between the two hemispheres. The negative sign in VMIX_{kpp} in the midlatitudes indicates a reduced magnitude of countergradient flux with depth in the boundary layer and the energy destruction from this effect can reach to 150 m near 40°. The mixing associated with diffusive fluxes (Fig. 9c) is predominant in the total mixing below 50 m in low-latitude regions. The large negative signal is located in the areas where isotherms are dominantly horizontal (see contours in Fig. 9c), suggesting a massive destruction of eddy energy by vertical turbulence in the tropics. The large vertical motions across the nearly horizontal isotherms are found to be primarily driven by vertical diffusion processes,

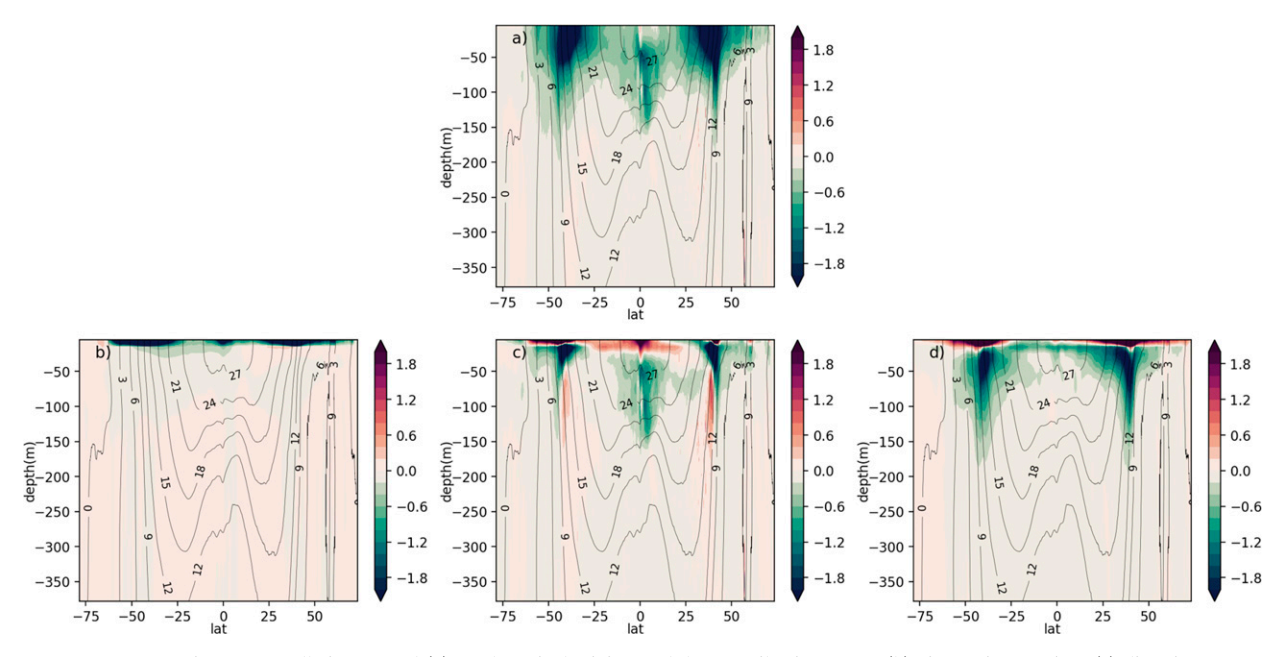


FIG. 9. Cross sections of zonally integrated (a) total vertical mixing and the contributions from (b) air–sea interaction, (c) diffusive flux, and (d) countergradient flux in KPP (${}^{\circ}$ C 2 m s $^{-1}$). The contour lines are mean temperature with a contour interval of 3 ${}^{\circ}$ C.

favoring water mass transformation in the tropical Pacific (Deppenmeier et al. 2021). Although the air-sea feedback is only concentrated near the surface, it comprises 52% of the total VMIX globally. If the energy dissipation that occurs through horizontal diffusion is also taken into account, the air-sea interactions induced by mesoscale structures contribute 39% of the global T-EPE destruction, which is close to a regional value (36%) in the Kuroshio Extension obtained from a coupled simulation by Yang et al. (2019). Note that we used an ocean-only model in this work, and there is no actual feedback from the ocean to the atmosphere. To make sure the air-sea interaction term in the forced simulation is reasonable, we compared VMIX_{a-s} in this work to that from a highresolution coupled simulation of the Community Earth System Model (CESM), which used the exact same ocean model as described in Small et al. (2014). The sink of T-EPE by mesoscale air-sea interaction is quite comparable in the ocean simulation used in this work to that in the coupled simulation with regard to both spatial distributions and global integrations (not shown).

e. Seasonality

There is evidence that the air–sea interactions at the oceanic mesoscale have pronounced seasonal signals due to strong turbulent heat fluxes that occur in the wintertime when atmospheric synoptic storms are active (Bishop et al. 2020; Yang et al. 2019; Ma et al. 2016). However, the impact of this seasonality on global eddy energetics has not yet been well addressed. Here, we examined how the seasonally varying mixing processes regulate the baroclinic energy pathway based on the T-EPE budgets. The depth-integrated distributions of the three-way balance between BC $_T^{\rm div}$, PKC $_T$ and VMIX in the upper 200 m are shown in Fig. 10 for the winter

months (JFM) and summer months (JAS) along with their corresponding zonal integrals. Globally, nearly identical spatial patterns are observed in BC_T^{div} for both seasons, and trivial differences are also found in their zonal distributions between the seasons, suggesting no obvious seasonality in the MPE-to-EPE conversions in the global ocean. Nevertheless, the subsequent conversion into EKE shows strong seasonal differences in terms of the horizontal distributions (Figs. 10c,d). In the midlatitudes, it is apparent that PKC_T is most prominent in the local summer season, implying a possible summer peak in EKE (Rieck et al. 2015). Moreover, the seasonal signal indicated by PKC_T is highly associated with the seasonality shown in VMIX (Figs. 10e,f). The weakened wintertime energy conversion in PKC_T is accompanied by the enhancement of vertical dissipation, and vice versa in summertime. Vertically, the cross sections of the zonally integrated terms are given in Fig. 11 for the two seasons. As shown in its horizontal distribution, a very weak seasonal signal is found in the vertical structure of BC_T^{div} . However, for the other two processes, PKC_T and VMIX, the vertical structures in the winter and summer are reversed between the two hemispheres. Furthermore, it is evident that the EKE conversion in the upper ocean is largely modulated by vertical mixing in different seasons. In the boreal wintertime (JFM), a deepened vertical structure of VMIX corresponds to a deeper core of PKC_T, where most of the energy above the core is destroyed through mixing. During the summertime (JAS), PKC_T reaches maximums at shallower depths due to the relatively weak mixing processes. The seasonality shown in Fig. 11 further provides evidence for the nearly three-way balance driving T-EPE variations. In addition, we compare the annual cycle of three dominant terms from the three regions shown as examples in Fig. 12. Each individual month displays a roughly

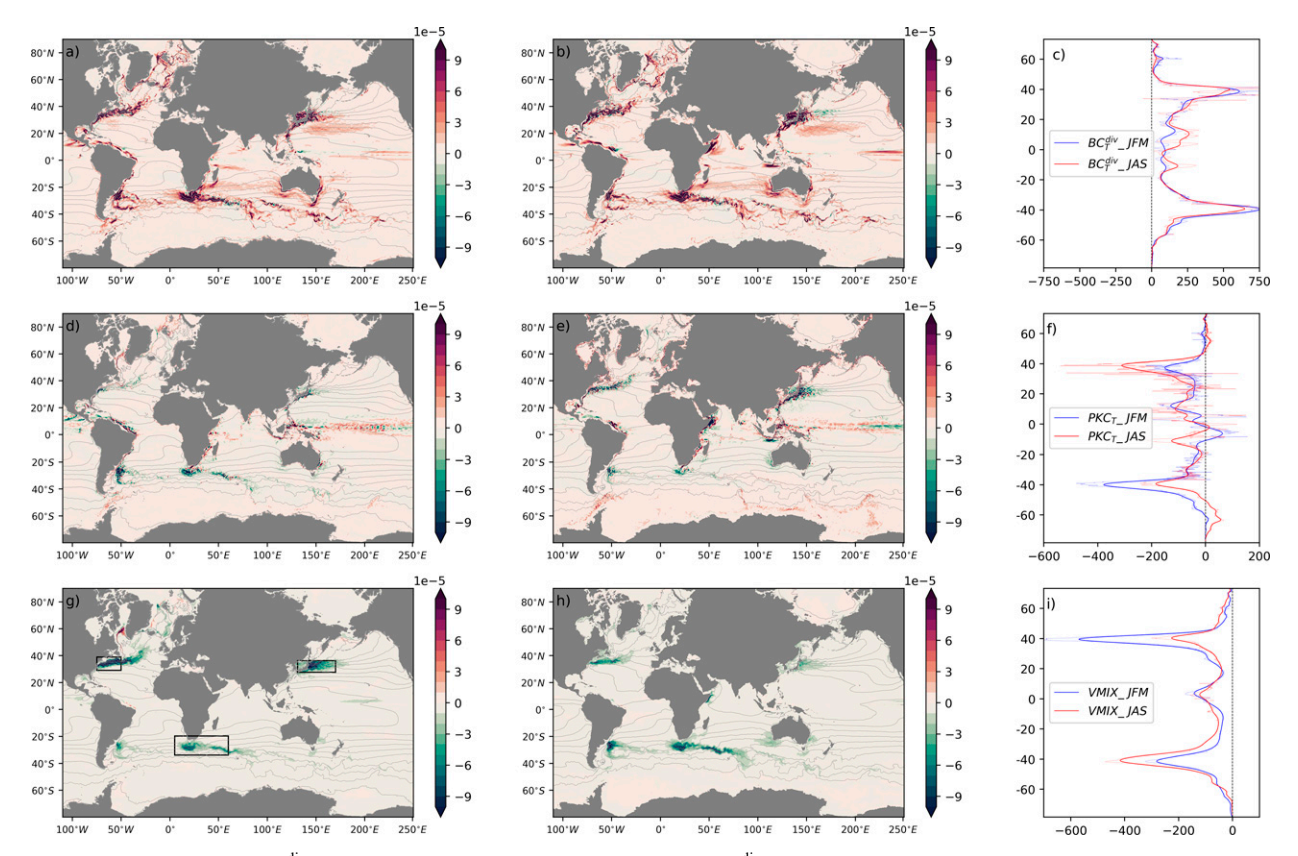


FIG. 10. Seasonality in BC $_T^{dv}$, PKC $_T$ and VMIX. (a),(b) Depth-integrated BC $_T^{dv}$ in the upper 200 m in the boreal winter (JFM) and summer (JAS), respectively (°C 2 m s $^{-1}$). (c) The corresponding zonal integrals are shown (°C 2 m 2 s $^{-1}$). (d)–(f) As in (a)–(c), but for PKC $_T$. (g)–(i) As in (a)–(c), but for VMIX. The gray contour lines are mean SST in the corresponding seasons with a contour interval of 3°C.

equivalent contribution (8%) of $\mathrm{BC}_T^{\mathrm{div}}$ over the year, and very small amplitudes of the annual cycles are found in $\mathrm{BC}_T^{\mathrm{div}}$ in all three regions. Inversely correlated signals appear in the annual variations between the regional PKC_T and VMIX, with the high summertime PKC_T corresponding to low VMIX. It is also indicated that PKC_T lags behind VMIX by 1–2 months in these regions. This phase relationship suggests a possible adjustment period of upper-ocean baroclinic instability to seasonally varying vertical dissipation.

4. Discussion and summary

In this study, we diagnosed the T-variance budgets from a global ocean model output over 20 years at high temporal (5-day) and horizontal (0.1°) resolutions. The global patterns of all dynamic processes that lead to T-EPE changes are explicitly established for the first time. For both the horizontal and vertical distributions the most prominent T-EPE variations are found in three main current systems: midlatitude western boundary currents, the Antarctic Circumpolar Current, and equatorial regions. In these highly turbulent regions, the generation of T-EPE is primarily attributed to downgradient horizontal eddy heat fluxes, as would be expected for baroclinic turbulence. The loss of T-EPE largely

occurs through its conversion into EKE and by dissipation due to mixing processes.

As the largest source of T-EPE generation in the ocean interior, the downgradient eddy heat fluxes (BC $_T$) are separated into rotational and divergent components by performing a Helmholtz decomposition on the 1/10° global grid. The BC_T estimates, which were improved by removing the nondivergent component, produces cross-isotherm divergent eddy heat fluxes with a smoothed global pattern. Based on global structures (Figs. 2d,e and 4d,e), BC_T^{div} is found to share large spatial coherence with PKC_T in the ocean interior. Locally, as in the western boundary currents, BC_T^{rot} has a similar spatial distribution to that of advection, and both of these terms have a component oriented up/down the mean thermal gradient along the meandering jets. These structures in BC_T^{rot} and ADV can thus compensate for each other to a large extent, but these compensations do not strictly achieve the balance of advection and BC_T^{rot} due to the presence of nontrivial eddy advection. Globally, the BC_T^{rot} , ADV, and HDIFF have relatively small contributions to the globally integrated energy balance, and the dominant processes in the T-variance equation are BC_T^{div} , PKC_T , and VMIX. It is found that positive baroclinic conversion can be largely balanced by upgradient vertical heat fluxes and vertical mixing.

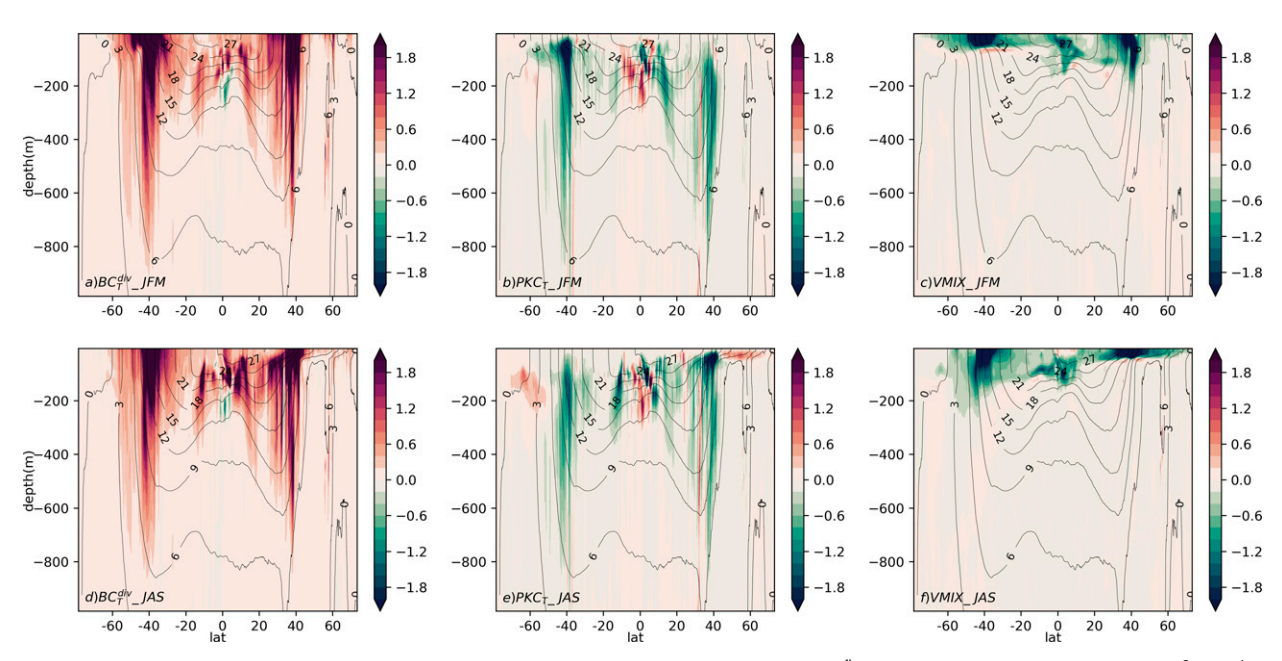


FIG. 11. Vertical structures of the budget terms in (top) JFM and (bottom) JAS for (a),(d) BC_T^{div} ; (b),(e) PKC_T ; and (c),(f) VMIX (°C² m s⁻¹). The gray contour lines are mean temperature in the corresponding seasons with a contour interval of 3°C.

Notably, we only considered the thermal contribution to EPE budget in this work. To evaluate the extent to which EPE variation can be explained by temperature variability, we multiply Eq. (5) by $\rho_o g^2 \alpha_\theta^2/N_r^2$ to obtain quantities that are proportional to the rate of EPE change in units of watts per cubic meter (W m⁻³). In doing so, the baroclinic conversion is found to account for about 0.8 TW of the global EPE generation, and approximately 0.5 TW of that total can then be converted to EKE through baroclinic instability. The other 0.3 TW of EPE converted from MPE is dissipated through air-sea interactions and oceanic interior mixing processes. The other processes are found to play less significant roles in regulating T-EPE variations and have small impacts on the dominant balance. In Marshall and Shutts (1981), there tends to be a one-to-one balance for energy conversions through MPE and EKE reservoirs in the adiabatic system. However, in reality, the presence of diabatic processes in the air-sea interface and ocean interior can augment this one-to-one balance by destroying EPE that would typically be available for

conversion to EKE. Based on the global diagnostics of the T-variance equation, the exchange between EPE and EKE reservoirs is approximately 40% weaker than that between MPE and EPE reservoirs, with the air-sea feedback and interior mixing playing nearly comparable roles in destroying T-EPE. This result implies that baroclinic instability in reality is not 100% efficient; in the POP model used in this work, it has an approximately 60% efficiency for converting MPE to EKE in the global system. Notably, in the regionally coupled model-based work in the Kuroshio Extension (Ma et al. 2016), energy dissipation is shown to account for more than 70% of the EPE in the upper 250 m. Because most dissipation occurs in the upper 200 m (Fig. 4f) but the eddy flux can reach to as deep as 800 m (Figs. 4d,e), it is not surprising that the regional ratio of dissipation of EPE was larger in the upper ocean than the full-depth analysis conducted in this work.

In addition to the mean state of the global *T*-EPE budgets, we further examined the seasonality in the dominant balance.

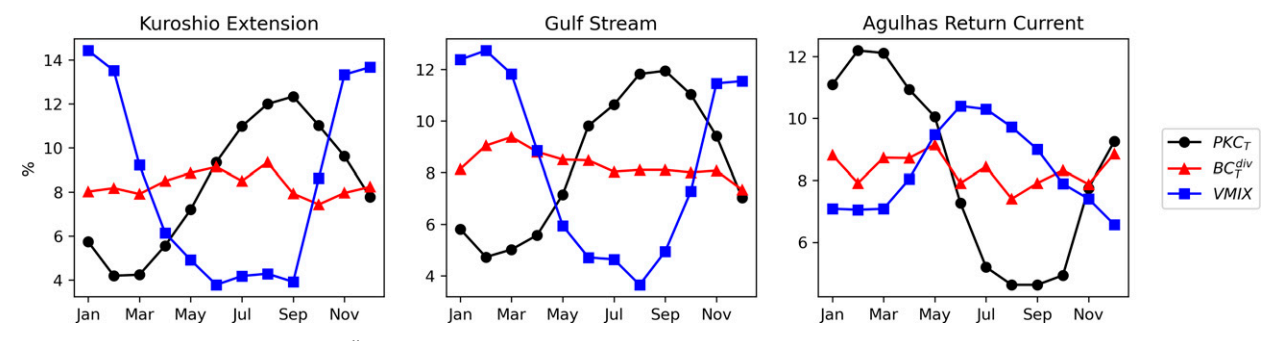


FIG. 12. Seasonal variations of BC_T^{dv} , PKC_T, and VMIX in the (a) Kuroshio Extension, (b) Gulf Stream, and (c) Agulhas Current, as indicated by boxes in Fig. 10. The y axis represents percentage of variance explained in each individual month over the year.

Previous studies have demonstrated the seasonal signal in upper-ocean EKE with mesoscale-resolving global coupled and uncoupled models (Uchida et al. 2017; Rieck et al. 2015). In terms of the energy conversions in the baroclinic pathway, strong seasonality is revealed in the conversion from EPE to EKE (PKC_T) in the upper ocean (Figs. 10 and 11). One implication of the seasonal difference in PKC_T refers to a possible mechanism explaining the seasonality of EKE, in which the seasonally varying baroclinic instability is a primary driver of the seasonality in upper-ocean EKE (Uchida et al. 2017; Kang et al. 2016). PKC_T reaches maximums in the local summer season in both hemispheres (Fig. 10), highly corresponding to the summer EKE peak, as demonstrated globally in Rieck et al. (2015). This summertime enhancement of eddy energy might be associated with the high occurrence of warm core rings in energetic regions such as the Gulf Stream (Gangopadhyay et al. 2019). In contrast with Uchida et al. (2017), who used the vertical eddy buoyancy flux to measure the generation of EKE, we estimated the strength of EKE conversion in the baroclinic pathway by the product of vertical eddy heat flux and the background thermal gradient (PKC $_T$). In addition, we note that the eddy flux alone instead reaches minimum values in the summer (not shown), which is consistent with what was demonstrated in Uchida et al. (2017). However, the background buoyancy is strongest in the summertime when the mixed layer is shallower. This strong stratification that occurs during the summer season can overcome the weak eddy buoyancy flux and result in large energy conversions and strong EKE. This indicates the importance of taking the variation of stratification into account when analyzing the seasonality in upper-ocean baroclinic instability. Zhai et al. (2008) further suggested that dissipation processes can drive seasonal variabilities in the surface EKE in the Gulf Stream, with weaker dissipation occurring in boreal summer. From the global patterns shown in Figs. 10 and 11, we showed that vertical mixing, which has a peak in the winter and is inversely related to the seasonality in PKC_T, can seasonally modulate the EPE–EKE conversion in baroclinic instability. Further spatial smoothing suggests that PKC_T is significantly (20%–30%) influenced by processes whose scales are smaller than 50 km but that BC_T, which is associated with the large-scale mean lateral temperature gradient, is virtually unchanged. The large impact of these smaller-scale structures on PKC_T suggests a high sensitivity of PKC_T to mixed layer processes and can partly reflect on the strongly correlated seasonality in the upper-ocean PKC $_T$ and VMIX.

The ocean components used in traditional climate models that do not resolve mesoscale eddies parameterize the impact of mesoscale variabilities on ocean circulation (Gent and McWilliams 1990). The Gent–McWilliams parameterization has been widely used in coarse resolution models; this parameterization scheme is energy-conserving and was developed under adiabatic conditions to mimic the MPE-to-EPE conversion due to baroclinic instability. Based on our analysis, the energy destruction that occurs due to strong air–sea interactions and interior mixing causes the global baroclinic instability to be much less efficient in reality. The mesoscale air–sea feedback alone can dissipate approximately 20% of the EPE resulting from baroclinic conversion,

according to our estimate obtained with the global high-resolution POP model. This significant sink effect on the ocean energetics will need to be considered in the future mesoscale parameterizations implemented in coarse resolution models. Furthermore, budget analysis also points to the importance of vertical interior mixing in modulating eddy energy dissipation, which may also need to be parameterized in climate models.

Acknowledgments. This work was supported by the National Science Foundation through Award 2023590 and by the National Center for Atmospheric Research (NCAR), which is a major facility sponsored by the National Science Foundation under Cooperative Agreement 1852977. The authors thank Justin Small, Lucas Cardoso Laurindo, Dhruv Balwada, and two anonymous reviewers for helpful comments that improved this work. We acknowledge computing and data storage resources provided by the Computational and Information System Laboratory (CISL) at NCAR. Guo thanks the support from the Advanced Study Program of NCAR.

Data availability statement. All datasets are publicly available. Sea surface height and geostrophic velocity data are archived online (http://marine.copernicus.eu). NOAA high resolution SST data are provided by the NOAA/OAR/ESRL PSL, Boulder, Colorado, from their website at https://psl.noaa.gov/. J-OFURO3 data are archived online (https://j-ofuro.isee.nagoya-u.ac.jp/en/). Model outputs from POP are archived on NCAR Campaign Storage and are available on request.

APPENDIX A

Derivation of *T***-EPE Equation**

The T-EPE equation [Eq. (1)] without partitioning BC term is derived from the temperature equation. The temperature (T) conservation equation for the model may be written as

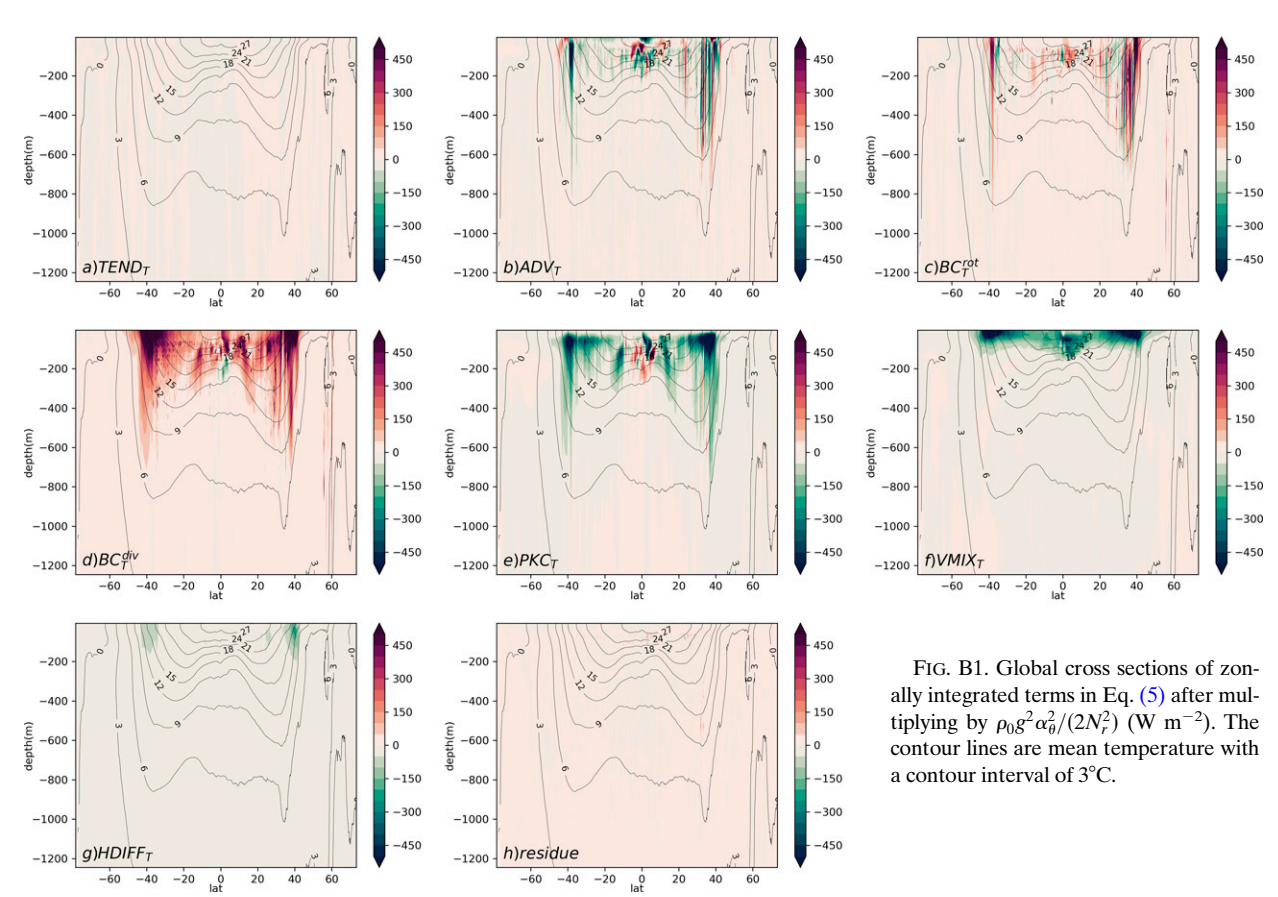
$$\frac{\partial T}{\partial t} = -\mathbf{u}_h \cdot \nabla_h T - w \frac{\partial T}{\partial z} + \frac{\partial}{\partial z} \left[\kappa \left(\frac{\partial T}{\partial z} - \Gamma \right) \right] + \frac{\partial}{\partial z} \left(\frac{Q_{\text{sw}}}{\rho_o C_p} \right) - A_h \nabla^4 T, \tag{A1}$$

with boundary condition

$$\left[\kappa \frac{\partial T}{\partial z}\right]_{z=0} = \frac{Q_o}{\rho_o C_p}.$$
 (A2)

To derive the T-variance equation, we first partition the T equation into mean and eddy components by applying the Reynolds decomposition on Eq. (A1), where mean quantities are denoted by an overbar and primes denote the deviations from the mean. Then the mean and eddy temperature equations are given as

$$\frac{\partial \overline{T}}{\partial t} = -\overline{\mathbf{u}}_h \cdot \nabla_h \overline{T} - \overline{w} \frac{\partial \overline{T}}{\partial z} + \frac{\partial}{\partial z} \left[\kappa \left(\frac{\partial \overline{T}}{\partial z} - \overline{\Gamma} \right) \right]
+ \frac{\partial}{\partial z} \left(\overline{Q}_{\text{sw}} \right) - A_h \nabla^4 \overline{T},$$
(A3)



$$\frac{\partial T'}{\partial t} = -\overline{\mathbf{u}}_{h} \cdot \nabla_{h} T' - \mathbf{u}'_{h} \cdot \nabla_{h} \overline{T} - \mathbf{u}'_{h} \cdot \nabla T' - \overline{w} \frac{\partial T'}{\partial z}
- w' \frac{\partial \overline{T}}{\partial z} - w' \frac{\partial T'}{\partial z} + \frac{\partial}{\partial z} \left[\kappa \left(\frac{\partial T'}{\partial z} - \Gamma' \right) \right]
+ \frac{\partial}{\partial z} \left(\frac{Q'_{\text{sw}}}{\rho_{\rho} C_{\rho}} \right) - A_{h} \nabla^{4} T'.$$
(A4)

Multiplying Eq. (A4) by T' and applying the $\overline{(\cdot)}$ operation gives the temperature variance budget as in Eq. (1),

$$\frac{\partial}{\partial t} \left(\frac{\overline{T'^2}}{2} \right) = -\overline{\mathbf{u}}_h \cdot \nabla_h \left(\frac{\overline{T'^2}}{2} \right) - \overline{\mathbf{u}}_h' \cdot \nabla \left(\frac{\overline{T'^2}}{2} \right) \\
- \overline{\mathbf{w}} \frac{\partial}{\partial z} \left(\frac{\overline{T'^2}}{2} \right) - \overline{\mathbf{w}}' \frac{\partial}{\partial z} \left(\frac{\overline{T'^2}}{2} \right) - \overline{\mathbf{u}}_h' \overline{T'} \cdot \nabla_h \overline{T} \\
- \overline{\mathbf{w}}' \overline{T'} \frac{\partial \overline{T}}{\partial z} + \overline{T'} \frac{\partial}{\partial z} \left[\kappa \left(\frac{\partial T'}{\partial z} - \Gamma' \right) \right] \\
+ \overline{T'} \frac{\partial}{\partial z} \left(\frac{Q'_{\text{sw}}}{\rho_c C_p} \right) - \overline{T'} A_h \nabla^4 T'. \tag{A5}$$

The first four terms on the right-hand side of Eq. (A5) indicates horizontal and vertical advection of T-variance

by mean and eddy velocities, and they can be further grouped into the total advection (ADV). Then we obtained the full *T*-EPE equation as shown in Eq. (1) before applying Helmholtz decomposition on eddy heat fluxes.

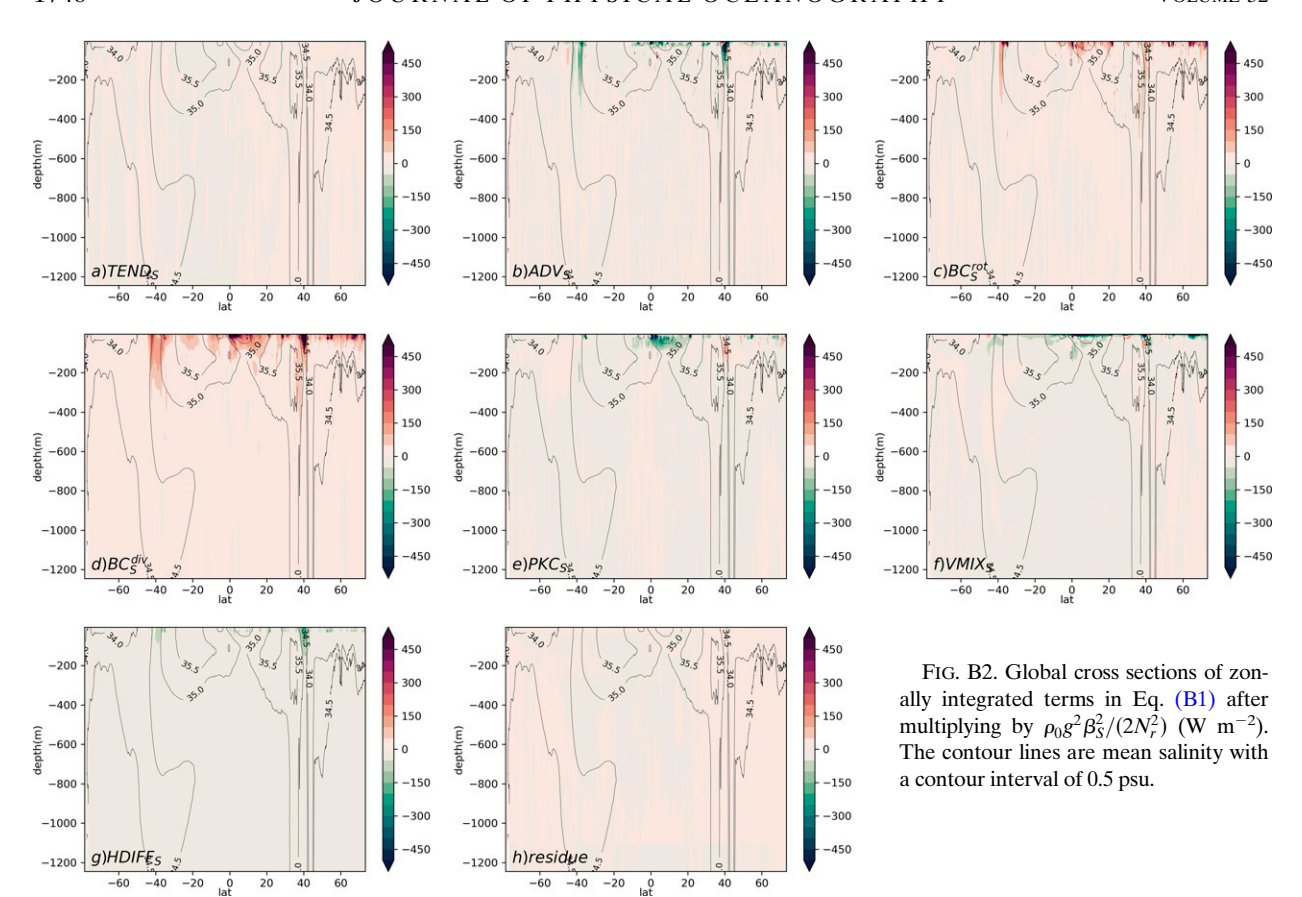
APPENDIX B

Temperature Variance Budget versus Salinity Variance Budget

To evaluate the relative importance of temperature and salinity variance to the global EPE budget, we write the salinity variance equation as follows, which is analogous to the temperature variance equation discussed in this work:

$$\frac{\frac{\partial}{\partial t} \left(\overline{S'^{2}} \right)}{\frac{\partial}{\partial t} \left(\overline{S'^{2}} \right)} = \underbrace{-\overline{\mathbf{u}'_{h}S'}^{\text{rot}} \cdot \nabla_{h} \overline{S}}_{\text{BC}_{S}^{\text{rot}}} \underbrace{-\overline{\mathbf{u}'_{h}S'}^{\text{div}} \cdot \nabla_{h} \overline{S}}_{\text{BC}_{S}^{\text{div}}} \underbrace{-\overline{\mathbf{w}'S'}}_{\text{PKC}_{S}} \underbrace{\frac{\partial \overline{S}}{\partial z}}_{\text{PKC}_{S}}$$

$$\underbrace{-\mathbf{v} \cdot \nabla \left(\overline{S'^{2}} \right)}_{\text{ADV}_{S}} + \underbrace{S' \frac{\partial}{\partial z} \left[\kappa \left(\frac{\partial S'}{\partial z} - \Gamma' \right) \right]}_{\text{VMIX}_{S}} \underbrace{-\overline{\mathbf{S}'A_{S}} \nabla^{4} S'}_{\text{HDIFF}_{S}}, \tag{B1}$$



with surface boundary condition

$$\left[\kappa \frac{\partial S'}{\partial z}\right]_{z=0} = S_{\text{ref}}(E' - P'), \tag{B2}$$

where S is the salinity, E is evaporation, P is precipitation, and $S_{\text{ref}} = 34.7$ psu is a constant reference salinity used to convert freshwater fluxes to a virtual salt flux in the model.

The eddy potential energy for a Boussinesq fluid can be expressed as EPE = $\left[\rho_0/(2N_r^2)\right]\overline{b'^2}$, where ρ_0 is a background density and N_r is a background buoyancy gradient. $b'=g[1-(\rho'/\rho_0)]$ denotes the buoyancy anomaly after considering the reference state and Reynolds decomposition of buoyancy field b. Using a linear equation of state for seawater, buoyancy anomaly can be expressed as $b'\approx \alpha_\theta gT'+\beta_S gS'$, and we can approximate EPE with temperature variance and salinity variance as

EPE
$$\approx \frac{\rho_0 g^2}{2N_r^2} \alpha_\theta^2 \overline{T'^2} + \frac{\rho_0 g^2}{2N_r^2} \beta_s^2 \overline{S'^2},$$
 (B3)

where α_{θ} and β_{S} denote the thermal expansion coefficient and salinity contraction coefficient, respectively, and these

two spatially variant coefficients are retrieved following McDougall et al. (2003).

In this section, we aim to examine the significance of the saline contribution to the global EPE budget relative to its thermal counterpart by comparing the globally integrated temperature and salinity variance budgets as derived in Eqs. (5) and (B1). To make Eqs. (5) and (B1) proportional to the rate of EPE variation in units of watts per cubic meter $(W m^{-3})$, we multiplied Eqs. (5) and (B1) by $\rho_0 g^2 \alpha_\theta^2/(2N_r^2)$ and $\rho_0 g^2 \beta_S^2/(2N_r^2)$ following Eq. (B3). The zonally integrated temperature and salinity variance budgets are shown in Figs. B1 and B2 with uniform scales and units. Note that Fig. B1 is the same as Fig. 4 except for the normalization by $\rho_0 g^2 \alpha_\theta^2 / (2N_r^2)$. The temperature variance budgets in Fig. B1 clearly display their dominant contributions to the EPE budget, while the magnitude of salinity variance budgets (Fig. B2) is relatively small and can be neglected in most regions. The only clearly salinity-dominant region is in the Arctic Ocean (see north of 40°N in Fig. B2), where the temperature has a weaker effect, even though salinity variance terms are intensified only at the surface levels at high latitudes. The signs and relationships between terms shown in the global salinity variance budget are found to be

consistent with what was discussed in the temperature variance budget in section 3. Considering the predominantly small contribution from salinity, we omit the saline effect and use the temperature variance equation as the proxy for the EPE equation in this work. Our study using the temperature variance equation follows previous observation-based studies of mesoscale air—sea exchange (Bishop et al. 2020) and baroclinic conversion rates (Guo and Bishop 2022), where both of these works focused on the thermal component of the EPE.

REFERENCES

- Abernathey, R., and P. Cessi, 2014: Topographic enhancement of eddy efficiency in baroclinic equilibration. *J. Phys. Oceanogr.*, **44**, 2107–2126, https://doi.org/10.1175/JPO-D-14-0014.1.
- —, and C. Wortham, 2015: Phase speed cross spectra of eddy heat fluxes in the eastern Pacific. J. Phys. Oceanogr., 45, 1285–1301, https://doi.org/10.1175/JPO-D-14-0160.1.
- Adcroft, A., C. Hill, and J. Marshall, 1997: Representation of topography by shaved cells in a height coordinate ocean model. *Mon. Wea. Rev.*, **125**, 2293–2315, https://doi.org/10.1175/1520-0493(1997)125<2293:ROTBSC>2.0.CO;2.
- Aoki, K., S. Minobe, Y. Tanimoto, and Y. Sasai, 2013: Southward eddy heat transport occurring along southern flanks of the Kuroshio Extension and the Gulf Stream in a 1/10° global ocean general circulation model. *J. Phys. Oceanogr.*, 43, 1899–1910, https://doi.org/10.1175/JPO-D-12-0223.1.
- Bishop, S. P., and F. O. Bryan, 2013: A comparison of mesoscale eddy heat fluxes from observations and a high-resolution ocean model simulation of the Kuroshio extension. *J. Phys. Oceanogr.*, **43**, 2563–2570, https://doi.org/10.1175/JPO-D-13-0150.1.
- —, D. R. Watts, and K. A. Donohue, 2013: Divergent eddy heat fluxes in the Kuroshio Extension at 144°–148°E. Part I: Mean structure. *J. Phys. Oceanogr.*, 43, 1533–1550, https://doi.org/10.1175/JPO-D-12-0221.1.
- —, R. J. Small, F. O. Bryan, and R. A. Tomas, 2017: Scale dependence of midlatitude air–sea interaction. *J. Climate*, **30**, 8207–8221, https://doi.org/10.1175/JCLI-D-17-0159.1.
- —, and —, 2020: The global sink of available potential energy by mesoscale air-sea interaction. *J. Adv. Model. Earth Syst.*, **12**, e2020MS002118, https://doi.org/10.1029/2020MS002118.
- Boyer, T. P., and Coauthors, 2013: World Ocean Database 2013. NOAA Atlas NESDIS 72, 208 pp., https://doi.org/10.25607/ OBP-1454.
- Bryan, F., and S. Bachman, 2015: Isohaline salinity budget of the North Atlantic salinity maximum. *J. Phys. Oceanogr.*, **45**, 724–736, https://doi.org/10.1175/JPO-D-14-0172.1.
- Bryan, F. O., P. R. Gent, and R. Tomas, 2014: Can Southern Ocean eddy effects be parameterized in climate models? J. Climate, 27, 411–425, https://doi.org/10.1175/JCLI-D-12-00759.1.
- Chassignet, E. P., and Coauthors, 2020: Impact of horizontal resolution on global ocean–sea ice model simulations based on the experimental protocols of the Ocean Model Intercomparison Project phase 2 (OMIP-2). *Geosci. Model Dev.*, 13, 4595–4637, https://doi.org/10.5194/gmd-13-4595-2020.
- Chelton, D. B., P. Gaube, M. G. Schlax, J. J. Early, and R. M. Samelson, 2011: The influence of nonlinear mesoscale eddies on near-surface oceanic chlorophyll. *Science*, 334, 328–332, https://doi.org/10.1126/science.1208897.

- Chen, R., G. R. Flierl, and C. Wunsch, 2014: A description of local and nonlocal eddy-mean flow interaction in a global eddy-permitting state estimate. J. Phys. Oceanogr., 44, 2336– 2352, https://doi.org/10.1175/JPO-D-14-0009.1.
- Cronin, M., and D. R. Watts, 1996: Eddy-mean flow interaction in the Gulf Stream at 68°W. Part I: Eddy energetics. J. Phys. Oceanogr., 26, 2107-2131, https://doi.org/10.1175/1520-0485(1996)026<2107:EFIITG>2.0.CO;2.
- Deppenmeier, A.-L., F. O. Bryan, W. S. Kessler, and L. Thompson, 2021: Modulation of cross-isothermal velocities with ENSO in the tropical Pacific cold tongue. *J. Phys. Oceanogr.*, 51, 1559– 1574, https://doi.org/10.1175/JPO-D-20-0217.1.
- Farneti, R., T. L. Delworth, A. J. Rosati, S. M. Griffies, and F. Zeng, 2010: The role of mesoscale eddies in the rectification of the Southern Ocean response to climate change. J. Phys. Oceanogr., 40, 1539–1557, https://doi.org/10.1175/2010JPO4353.1.
- Ferrari, R., and C. Wunsch, 2009: Ocean circulation kinetic energy: Reservoirs, sources, and sinks. *Annu. Rev. Fluid Mech.*, 41, 253–282, https://doi.org/10.1146/annurev.fluid. 40.111406.102139.
- Gangopadhyay, A., G. Gawarkiewicz, E. N. S. Silva, M. Monim, and J. Clark, 2019: An observed regime shift in the formation of warm core rings from the Gulf Stream. *Sci. Rep.*, 9, 12319, https://doi.org/10.1038/s41598-019-48661-9.
- Gent, P. R., and J. C. McWilliams, 1990: Isopycnal mixing in ocean circulation models. *J. Phys. Oceanogr.*, **20**, 150–155, https://doi.org/10.1175/1520-0485(1990)020<0150: IMIOCM>2.0.CO;2.
- Griffies, S. M., and Coauthors, 2015: Impacts on ocean heat from transient mesoscale eddies in a hierarchy of climate models. J. Climate, 28, 952–977, https://doi.org/10.1175/JCLI-D-14-00353.1.
- Guo, Y., and S. Bishop, 2022: Surface divergent eddy heat fluxes and their impacts on mixed layer eddy-mean flow interactions. J. Adv. Model. Earth Syst., 14, e2021MS002863, https:// doi.org/10.1029/2021MS002863.
- Jayne, S. R., and J. Marotzke, 2002: The oceanic eddy heat transport. *J. Phys. Oceanogr.*, 32, 3328–3345, https://doi.org/10.1175/1520-0485(2002)032<3328:TOEHT>2.0.CO;2.
- Johnson, B. K., F. O. Bryan, S. A. Grodsky, and J. A. Carton, 2016: Climatological annual cycle of the salinity budgets of the subtropical maxima. *J. Phys. Oceanogr.*, 46, 2981–2994, https://doi.org/10.1175/JPO-D-15-0202.1.
- Kang, D., and E. N. Curchitser, 2015: Energetics of eddy-mean flow interactions in the Gulf Stream region. J. Phys. Oceanogr., 45, 1103–1120, https://doi.org/10.1175/JPO-D-14-0200.1.
- —, and A. Rosati, 2016: Seasonal variability of the Gulf Stream kinetic energy. *J. Phys. Oceanogr.*, 46, 1189–1207, https://doi.org/10.1175/JPO-D-15-0235.1.
- Killworth, P. D., 1992: An equivalent-barotropic mode in the fine resolution Antarctic model. J. Phys. Oceanogr., 22, 1379–1387, https://doi.org/10.1175/1520-0485(1992)022<1379: AEBMIT>2.0.CO;2.
- Klocker, A., and R. Abernathey, 2014: Global patterns of mesoscale eddy properties and diffusivities. J. Phys. Oceanogr., 44, 1030–1046, https://doi.org/10.1175/JPO-D-13-0159.1.
- Kobayashi, S., and Coauthors, 2015: The JRA-55 reanalysis: General specifications and basic characteristics. J. Meteor. Soc. Japan, 93, 5–48, https://doi.org/10.2151/jmsj.2015-001.
- Large, W. G., J. C. McWilliams, and S. C. Doney, 1994: Oceanic vertical mixing: A review and a model with a nonlocal boundary layer parameterization. *Rev. Geophys.*, 32, 363–403, https://doi.org/10.1029/94RG01872.

- Lorenz, E. N., 1955: Available potential energy and the maintenance of the general circulation. *Tellus*, 7, 157–167, https:// doi.org/10.3402/tellusa.v7i2.8796.
- Luecke, C., and Coauthors, 2017: The global mesoscale eddy available potential energy field in models and observations. J. Geophys. Res. Oceans, 122, 9126–9143, https://doi.org/10. 1002/2017JC013136.
- Ma, X., and Coauthors, 2016: Western boundary currents regulated by interaction between ocean eddies and the atmosphere. *Nature*, 535, 533–537, https://doi.org/10.1038/nature18640.
- Marshall, J., and G. Shutts, 1981: A note on rotational and divergent eddy fluxes. *J. Phys. Oceanogr.*, **11**, 1677–1680, https://doi.org/10.1175/1520-0485(1981)011<1677:ANORAD>2. 0 CO-2
- McDougall, T. J., D. R. Jackett, D. G. Wright, and R. Feistel, 2003: Accurate and computationally efficient algorithms for potential temperature and density of seawater. *J. Atmos. Oceanic Technol.*, 20, 730–741, https://doi.org/10.1175/1520-0426(2003)20<730:AACEAF>2.0.CO;2.
- Pacanowski, R. C., and A. Gnanadesikan, 1998: Transient response in a z-level ocean model that resolves topography with partial cells. *Mon. Wea. Rev.*, 126, 3248–3270, https://doi.org/10.1175/1520-0493(1998)126<3248:TRIAZL>2.0.CO;2.
- Reynolds, R. W., T. M. Smith, C. Liu, D. B. Chelton, K. S. Casey, and M. G. Schlax, 2007: Daily high-resolution-blended analyses for sea surface temperature. *J. Climate*, 20, 5473–5496, https://doi.org/10.1175/2007JCL11824.1.
- Rieck, J. K., C. W. Böning, R. J. Greatbatch, and M. Scheinert, 2015: Seasonal variability of eddy kinetic energy in a global high-resolution ocean model. *Geophys. Res. Lett.*, 42, 9379– 9386, https://doi.org/10.1002/2015GL066152.
- Small, R. J., and Coauthors, 2014: A new synoptic scale resolving global climate simulation using the Community Earth System Model. J. Adv. Model. Earth Syst., 6, 1065–1094, https://doi. org/10.1002/2014MS000363.
- Smith, K. S., 2007: The geography of linear baroclinic instability in Earth's oceans. J. Mar. Res., 65, 655–683, https://doi.org/10. 1357/002224007783649484.

- Smith, R., and Coauthors, 2010: The Parallel Ocean Program (POP) reference manual ocean component of the Community Climate System Model (CCSM) and Community Earth System Model (CESM). Doc. LAUR-10-01853, 140 pp., https://www.cesm.ucar.edu/models/cesm1.0/pop2/doc/sci/POPRefManual.pdf.
- Tomita, H., T. Hihara, S. Kako, M. Kubota, and K. Kutsuwada, 2019: An introduction to J-OFURO3, a third-generation Japanese ocean flux data set using remote-sensing observations. *J. Oceanogr.*, 75, 171–194, https://doi.org/10.1007/ s10872-018-0493-x.
- Tsujino, H., and Coauthors, 2018: JRA-55 based surface dataset for driving ocean–sea-ice models (JRA55-do). *Ocean Modell.*, **130**, 79–139, https://doi.org/10.1016/j.ocemod.2018.07.002.
- Uchida, T., R. Abernathey, and S. Smith, 2017: Seasonality of eddy kinetic energy in an eddy permitting global climate model. *Ocean Modell.*, 118, 41–58, https://doi.org/10.1016/j. ocemod.2017.08.006.
- Volkov, D. L., T. Lee, and L.-L. Fu, 2008: Eddy-induced meridional heat transport in the ocean. *Geophys. Res. Lett.*, 35, L20601, https://doi.org/10.1029/2008GL035490.
- Von Storch, J.-S., C. Eden, I. Fast, H. Haak, D. Hernández-Deckers, E. Maier-Reimer, J. Marotzke, and D. Stammer, 2012: An estimate of the Lorenz energy cycle for the world ocean based on the STORM/NCEP simulation. *J. Phys. Oceanogr.*, 42, 2185–2205, https://doi.org/10.1175/JPO-D-12-079.1.
- Yang, H., P. Chang, B. Qiu, Q. Zhang, L. Wu, Z. Chen, and H. Wang, 2019: Mesoscale air–sea interaction and its role in eddy energy dissipation in the Kuroshio Extension. J. Climate, 32, 8659–8676, https://doi.org/10.1175/JCLI-D-19-0155.1.
- Zhai, X., and R. J. Greatbatch, 2006: Inferring the eddy-induced diffusivity for heat in the surface mixed layer using satellite data. *Geophys. Res. Lett.*, 33, L24607, https://doi.org/10.1029/ 2006GL027875.
- —, and J.-D. Kohlmann, 2008: On the seasonal variability of eddy kinetic energy in the Gulf Stream region. *Geophys. Res. Lett.*, 35, L24609, https://doi.org/10.1029/2008GL036412.